Cell Reports

Article

Activation of polo-like kinase 1 correlates with selective motor neuron vulnerability in familial ALS

Graphical abstract

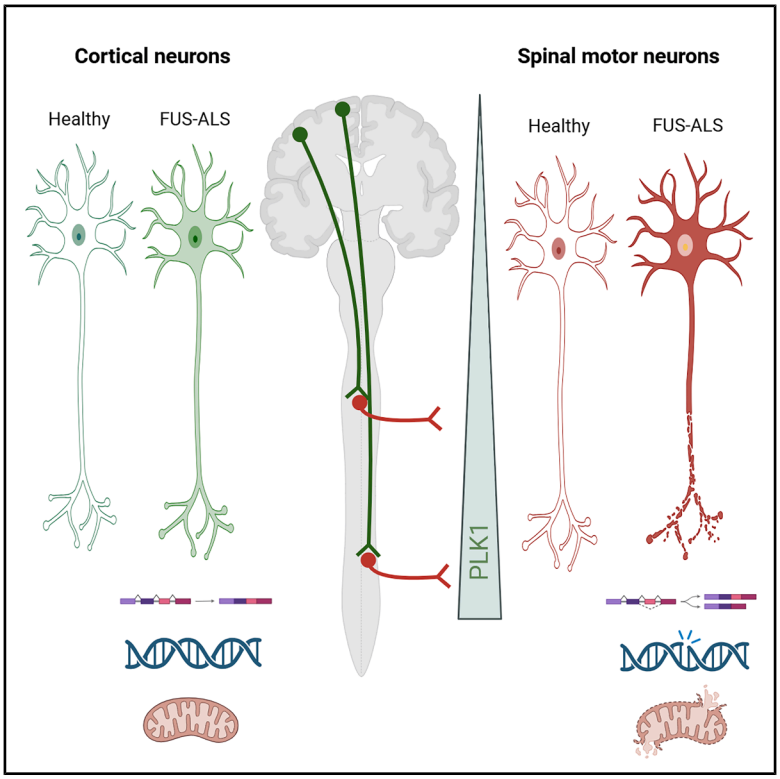

Authors

Barbara Szewczyk, Vitaly Zimyanin, Julia Japtok, ..., Brian J. Wainger, Anand Goswami, Andreas Hermann

Correspondence

andreas.hermann@med.uni-rostock.de

In brief

Szewczyk et al. show that FUS-ALS primarily impacts spinal motor neurons rather than cortical neurons. This is due to a pronounced nuclear loss of FUS associated with impaired DNA damage response and missplicing leading to upregulation of PLK1 as a protective factor against genotoxicity in spinal motor neurons.

Highlights

- FUS-ALS primarily impacts spinal motor neurons rather than cortical neurons
- DNA damage and cell cycle regulators are increased in sMNs, with PLK1 being central
- Nuclear loss of FUS is particularly high in sMNs and correlates to DNA damage
- PLK1 upregulation is common in all major fALS

Szewczyk et al., 2025, Cell Reports *44*, 116113
September 23, 2025
https://doi.org/10.1016/j.celrep.2025.116113

CellPress

Cell Reports

CellPress
OPEN ACCESS

Article

Activation of polo-like kinase 1 correlates with selective motor neuron vulnerability in familial ALS

Barbara Szewczyk,[1] Vitaly Zimyanin,[13] Julia Japtok,[2] Aaron Held,[3] Arun Pal,[2,4] Dajana Großmann,[1] Hannes Glaß,[1] Alexandra V. Jürs,[1] Banaja P. Dash,[1] Maciek Bak,[5] Marcel Naumann,[1] Christiane Hartmann,[1] Olena Kuksenko,[6] René Günther,[2] Tzu-Ting Kao,[7,8] Katrin Sameith,[9] Andreas Dahl,[9] Jared Sterneckert,[10,11] Eleonora Aronica,[12] Neil A. Shneider,[7] Andreas Büttner,[14] Alberto Catanese,[15] Hemali Phatnani,[6] Markus Kipp,[16,19,20] Brian J. Wainger,[3,17,18] Anand Goswami,[7,8] and Andreas Hermann[1,19,20,21,*]

[1]Translational Neurodegeneration Section "Albrecht Kossel", Department of Neurology, Rostock University Medical Center, Rostock, Germany
[2]Department of Neurology, Technische Universität Dresden, Dresden, Germany
[3]Department of Neurology, Sean M. Healey & AMG Center for ALS, Massachusetts General Hospital, Boston, MA, USA
[4]Dresden High Magnetic Field Laboratory (HLD-EMFL), Helmholtz-Zentrum Dresden-Rossendorf (HZDR), 01328 Dresden, Germany
[5]CORE, Krakow, Poland
[6]Center for Genomics of Neurodegenerative Disease, New York Genome Center, New York, NY 10013, USA
[7]Department of Neurology, Center for Motor Neuron Biology and Disease, Columbia University, New York, NY 10032, USA
[8]Department of Neurology, Eleanor and Lou Gehrig ALS Center, Columbia University, New York, NY 10032, USA
[9]DRESDEN-concept Genome Center, Center for Molecular and Cellular Bioengineering (CMCB), Technische Universität Dresden, 01307 Dresden, Germany
[10]Centre for Regenerative Therapies TU Dresden, Technische Universität Dresden, Dresden, Germany
[11]Medical Faculty Carl Gustav Carus of TU Dresden, Dresden, Germany
[12]Department of (Neuro)Pathology, Amsterdam UMC, University of Amsterdam, Amsterdam Neuroscience, Amsterdam, the Netherlands
[13]Department of Molecular Physiology and Biological Physics and Center for Membrane and Cell Physiology, University of Virginia School of Medicine, Charlottesville, VA, USA
[14]Institute of Forensic Medicine, Rostock University Medical Center, 18055 Rostock, Germany
[15]Institute of Anatomy and Cell Biology, Ulm University, 89081 Ulm, Germany
[16]Institute for Anatomy, Rostock University Medical Center, Rostock, Germany
[17]Department of Anesthesiology, Critical Care and Pain Medicine, Massachusetts General Hospital, Boston MA 02114, USA
[18]Broad Institute of Harvard University and MIT, Cambridge, MA 02142, USA
[19]German Center for Neurodegenerative Diseases (DZNE) Rostock/Greifswald, Rostock, Germany
[20]Center for Transdisciplinary Neurosciences Rostock (CTNR), Rostock University Medical Center, Rostock, Germany
[21]Lead contact
*Correspondence: andreas.hermann@med.uni-rostock.de
https://doi.org/10.1016/j.celrep.2025.116113

SUMMARY

Mutations in the *Fused in Sarcoma* (*FUS*) gene cause familial amyotrophic lateral sclerosis (ALS), characterized by selective degeneration of spinal motor neurons (sMNs) with relative sparing of cortical neurons (CNs). The mechanisms underlying this cell-type vulnerability remain unclear. Here, we compare CNs and sMNs derived from FUS-ALS models to assess differential responses to FUS mutations. We find that CNs are less affected than sMNs in DNA damage repair, axonal organelle trafficking, and stress granule dynamics. RNA sequencing (RNA-seq) reveals distinct transcriptomic signatures, with sMNs uniquely activating DNA damage responses involving cell cycle regulators, particularly polo-like kinase 1 (PLK1). PLK1 is highly expressed in sMNs but not CNs, correlating with greater nuclear FUS loss and splicing defects in sMNs. Cross-comparison with other familial ALS RNA-seq datasets highlights PLK1 upregulation as a shared molecular feature. These findings identify intrinsic differences between CNs and sMNs in FUS-ALS and suggest PLK1 as a potential driver of sMN vulnerability.

INTRODUCTION

Amyotrophic lateral sclerosis (ALS) caused by mutations in *Fused in Sarcoma* (*FUS*) is one of the four most common genetic forms of ALS and is particularly prevalent in young cases. ALS is a progressive neurodegenerative disorder that mainly affects motor neurons, leading to muscle weakness, paralysis, and respiratory failure. In healthy cells, FUS is primarily nuclear and

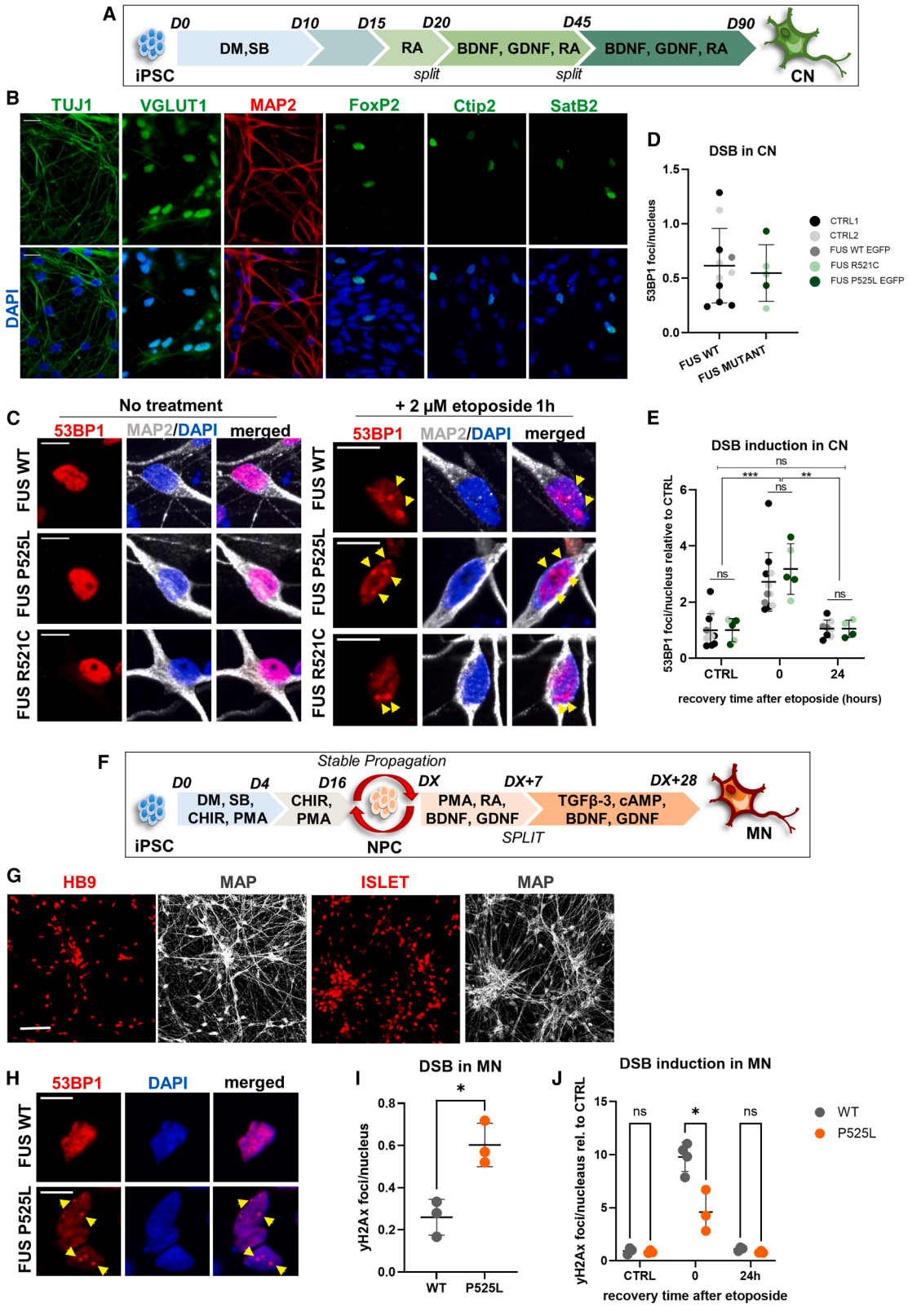

(legend on next page)

contributes to various cellular functions. FUS ALS-associated mutations, mostly located in the nuclear localization signal (NLS), impair nuclear import, leading to cytoplasmic accumulation and loss of nuclear function.[1,2]

The mechanisms by which FUS mutations cause selective motor neuron degeneration remain unclear. FUS is ubiquitously expressed and regulates transcription, splicing, RNA export, and the DNA damage response.[3,4] Both loss of nuclear function and gain of cytoplasmic function of FUS have been implicated in the pathology of FUS-ALS. Loss of nuclear FUS impairs recruitment to DNA damage sites and alters splicing of target transcripts,[5] while cytoplasmic FUS accumulation disrupts stress granule dynamics,[6] suppresses protein translation,[7] and impairs axonal organelle trafficking in motor neurons.[3,8]

Although FUS-ALS shares features with other forms of ALS—such as protein aggregation, disturbed RNA metabolism, impaired axonal transport, and DNA damage—it presents with distinct clinical features. While most forms of ALS lead to degeneration of both upper (cortical) and lower (spinal) motor neurons, FUS-ALS primarily affects spinal motor neurons and rarely involves cognitive impairment.[9] In contrast to other ALS forms, frontotemporal dementia with FUS aggregation (FTLD-FUS) and FUS-ALS seem to be two distinct diseases. FTLD-FUS is a sporadic disease without mutations in FUS, characterized by aggregation of the wild-type (WT) FUS, while FUS-ALS is caused by mutated FUS and associated with aggregation of both mutant and WT FUS.[10,11]

Here, we investigate the selective vulnerability of motor neurons in FUS-ALS using induced pluripotent stem cells (iPSCs)-derived cortical neurons (CNs) and spinal motor neurons (sMNs). This approach enables cell-type-specific analysis of early disease mechanisms in a genetically controlled environment.

RESULTS

Mutant FUS cortical neurons show fewer signs of increased DNA damage

DNA damage has gained attention as one of the major phenotypes linked to ALS.[12] Due to the role of FUS in DNA damage repair,[13] accumulation of DNA damage in sMNs has been studied extensively.[3,4] Considering that cortical neurons appear less affected in FUS-ALS than in other ALS types (e.g., TDP43-ALS),[9,14] we investigated whether FUS-ALS CNs show signs of DNA damage. We differentiated CNs from an isogenic pair of previously generated human induced pluripotent stem cells (hiPSCs) in which either WT or NLS mutant FUS P525L was tagged with EGFP using CRISPR/Cas9.[3] We also used a non-isogenic FUS WT and FUS R521C NLS mutant hiPSC (Naumann et al.[3]; all the cell lines are described in Table S1). CNs were considered mature after 90 days of differentiation (Figure 1A) and formed mixed cortical culture of neurons and astrocytes, with ~20% MAP2$^+$ neurons across genotypes (Figure S1), expressing different cortical layer markers (Figure 1B). We find no difference in double-strand breaks (DSBs) between WT and mutant FUS CNs (Figures 1C, left, and 1D). We then treated the cells for 1 h with 2 μM etoposide, which is a DNA-damage-inducing compound and analyzed them immediately or after 24 h of recovery (Figure 1C, right). 53BP1 puncta quantification shows significantly increased DSBs immediately after the treatment and recovery to baseline after 24 h of recovery, with no difference between WT and mutant FUS CNs (Figure 1E). CNs carrying a FUS mutation thus do not show increased DNA damage or impaired repair, in striking contrast to previous findings in sMNs.[3,4] We also analyzed DNA damage in sMNs derived from the same isogenic FUS WT and P525L cell lines. sMNs were generated using a small molecule-based approach[3,15] (Figure 1F), yielding cultures enriched in spinal motor neurons expressing typical markers characteristic for sMNs (Figure 1G). As previously reported, we observe significantly more DSBs in mutant than WT sMNs at baseline (Figures 1H and 1I), but fewer etoposide-induced DSB in mutants (Figure 1J). This side-by-side comparison indicates that CNs and sMNs derived from the same isogenic pair show different DNA damage responses FUS mutation.

FUS recruitment to DNA damage sites is less impaired by mutant FUS in cortical neurons than spinal motor neurons

FUS has been shown to be essential in DNA damage repair by rapidly recruiting to the damage site and regulating other repair components.[3,16,17] Therefore, we analyzed FUS recruitment dynamics to the damage site in CNs versus sMNs. We used UV-laser irradiation to induce DNA damage and live-cell imaging to track FUS-eGFP at laser-irradiated sites (Figure 2A). Both CNs and sMNs show WT FUS recruitment to damage sites (Figures 2B and 2D). P525L FUS is also robustly recruited in CNs, although its association and dissociation kinetics differ

Figure 1. Spinal motor neurons, but not cortical neurons, show increased DNA damage

Differentiation of patient-derived iPSCs to CNs (A–E) and sMNs (F–I) is shown.

(A) Schematic depiction of cortical neuron differentiation protocol.

(B) This protocol yields a mixed cortical culture containing mainly glutamatergic neurons from upper (FOXP2$^+$) and lower cortical layers (CTIP2$^+$; SATB2$^+$). Depicted are representative images.

(C–E) DNA double-strand breaks in postmitotic neurons were measured by evaluating 53BP1 in MAP2$^+$ neurons with and without etoposide treatment and recovery. Representative images of WT and mutants are depicted in (C). DNA DSBs per nucleus in untreated CNs are quantified in (D), while (E) shows DNA DSBs upon etoposide treatment and recovery normalized to the untreated condition.

(F) Schematic depiction of spinal motor neuron differentiation protocol.

(G) This protocol yields ISLET 1$^+$, HB9$^+$, and CHAT$^+$ sMNs. Depicted are representative images.

(H–J) DNA double-strand breaks in postmitotic neurons were measured by evaluating 53BP1/γH2A.X in MAP2$^+$ neurons with and without etoposide treatment and recovery (see also Figure S2B). DNA DSBs per nucleus in untreated sMNs are quantified in (I), while (J) shows DNA DSBs upon etoposide treatment and recovery normalized to the untreated condition. Representative images of WT are depicted in (H). Scale bar, 10 μm. Data on dot plots is presented as mean with SD. *$p \leq 0.05$, **$p \leq 0.01$, ***$p \leq 0.001$.

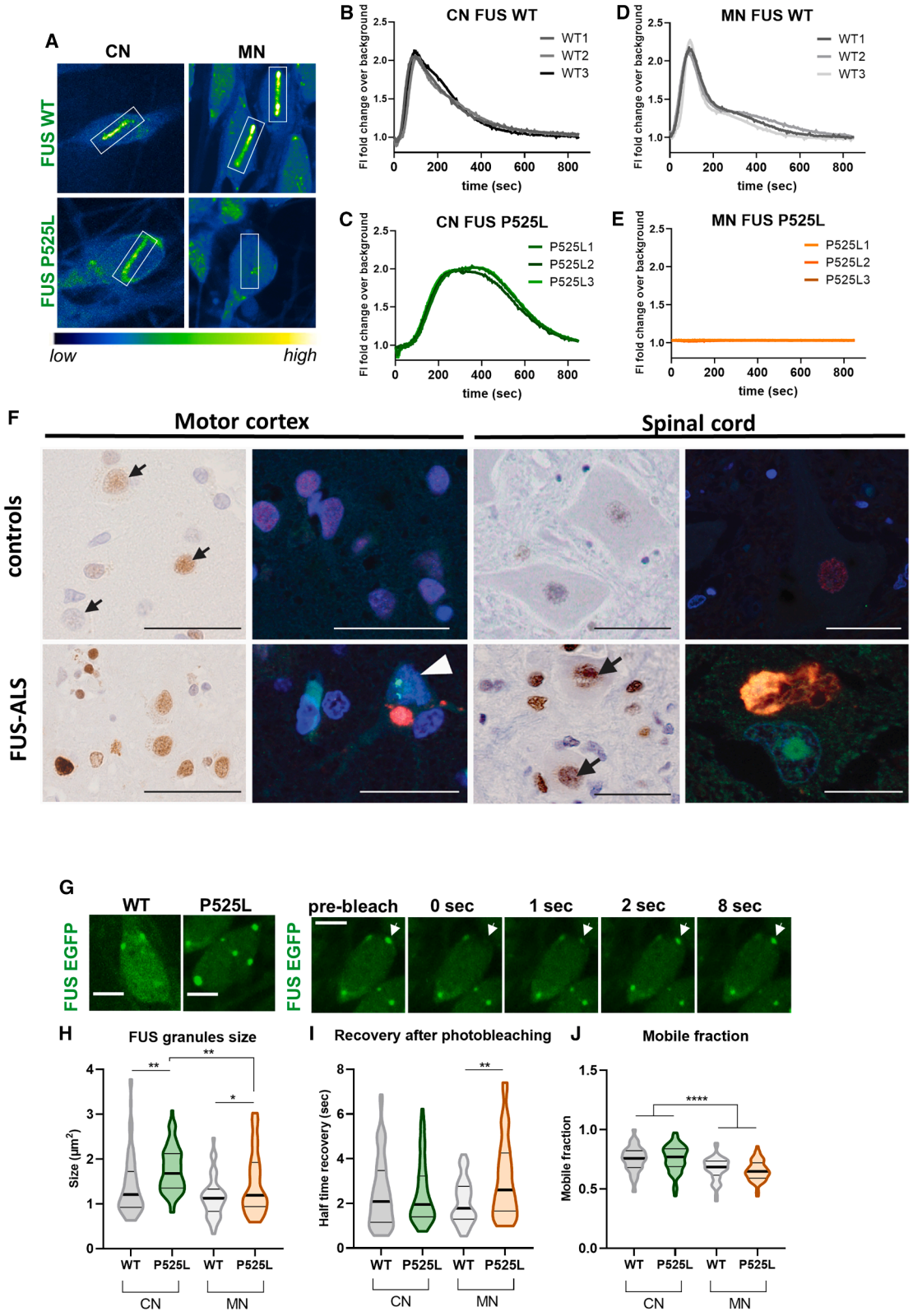

(legend on next page)

from those of WT (Figure 2C). In striking contrast, P525L FUS does not recruit to the damage site in sMNs, as previously reported[3] (Figure 2E). This suggests that FUS-dependent DNA damage repair is differently affected in CNs and sMNs in FUS-ALS.

DNA damage is consistently high in spinal but not cortical neurons in FUS-ALS

To validate these findings, we analyzed autopsy tissue from patients with FUS-ALS (Table S2), including frontal and motor cortex and lumbar spinal cord from the same patients and controls. Consistent with previous findings,[3] lumbar α-MN from patients with FUS-ALS shows strong γH2A.X immunoreactivity in the nucleus (Figures 2F and S2, black arrows) compared to age-matched controls. Co-immunolabeling reveals γH2AX accumulations co-localizing with cytoplasmic FUS aggregates in the cytoplasm of surviving α-MN and increased nuclear γH2AX (Figures 2F and S3). Given γH2AX immunoreactivity as a DSB marker and neurodegenerative feature, we assessed CNs of the same patients. Betz cells and CNs from controls show minimal γH2AX immunoreactivity (black arrows), while in FUS-ALS the staining is variable (Figures 2F, S2, and S3). Unlike the sMNs, most CNs show mild to moderate γH2AX; only 30%–40% of CNs display strong immunoreactivity comparable to sMNs (quantified in Table S3). Similar to lumbar α-MN, increased γH2AX (Figure 2Fwhite arrow) co-occurs with FUS aggregates. Overall, we found that DNA damage is not a consistent feature in FUS-ALS CNs.

Stress granule dynamics is less disrupted by mutant FUS in cortical neurons than spinal motor neurons

Since FUS recruitment to the DNA damage site is regulated by liquid-liquid phase separation (LLPS),[17,18] we next analyzed whether other LLPS-related FUS processes differ between CNs and sMNs. We focus on stress granules (SGs), which are FUS-containing cytosolic biocondensates formed via LLPS under stress.[19] We previously showed that in P525L FUS sMNs, liquid-like properties of SGs are disturbed.[7] We stressed the cells with sodium arsenite to induce SGs and evaluated FUS-EGFP-positive SGs using fluorescence recovery after photo bleaching (FRAP) (Figures 2G and S4). P525L FUS granules are larger than WT in both CNs and sMNs (Figure 2H). However, half-time fluorescence recovery is not changed in P525L CNs compared to WT, but it is reduced in sMNs (Figure 2I). SG mobile fraction is also significantly lower in sMNs than CNs, with no difference between WT and P525L FUS (Figure 2J).

Mutant FUS cortical neurons exhibit less axonal organelle trafficking disruption than spinal motor neurons

DNA damage accumulation in FUS ALS sMNs is reported as an upstream event in the disease progression and a driver of other phenotypes, such as impaired axonal organelle trafficking.[3] We next assessed whether organelle trafficking is also affected in CNs. We cultured CNs and sMNs in microfluidic chambers and performed live cell imaging using MitoTracker Deep Red or LysoTracker red to label mitochondria and lysosomes in proximal and distal axons (Figures 3A and S5). There is no change in the mean speed of either organelle in mutant FUS CNs in both axon regions (Figures 3B and 3C). Mitochondrial track displacement is also unchanged, while lysosomes show a slight but significant increase of track displacement in distal axon—still markedly lower than WT sMNs (Figures 3D and 3E). In contrast, mutant FUS sMNs exhibit a strong decline in mean speed and track displacement of both organelles, particularly distally (Figures 3F–3I). These results indicate that CNs do not display phenotypes typical of FUS ALS sMNs.

RNA sequencing of FUS ALS cortical and spinal motor neurons reveals fundamental transcriptomic differences

To understand the molecular basis of the phenotypical differences between CNs and sMNs, we performed RNA sequencing (RNA-seq). We differentiated CNs and sMNs as

Figure 2. Mutant FUS differentially affects FUS dynamics in spinal motor neurons vs. cortical neurons

(A) Isogenic sMNs or CNs expressing either wild-type (FUS WT) or mutant P525L FUS-eGFP (FUS P525L) were matured for 21 DIV after final splitting, as detailed in the STAR Methods. Recruitment and withdrawal of FUS-eGFP at linear UV laser-induced DNA damage sites in nuclei (boxed area) were imaged live. Shown are representative single movie frames at 150 s, corresponding to the approximate peak of eGFP. The eGFP intensity is shown in the LUT "green fire blue" of the FIJI software; i.e., low eGFP intensities are shown in blue and high intensities in green; no nuclear stain was used. Note failed recruitment in FUS P525L sMNs compared to FUS WT; CNs showed normal recruitment of both WT and mutant FUS variant. In case of failed FUS P525L recruitment in MNs, the laser beam left a dark line due to photobleaching, not to be mistaken with FUS-eGFP withdrawal from the DNA damage site.

(B–E) Quantification of (A). Note the failed recruitment of FUS P525L sMNs (E, orange curves) over the entire 850-s recording period, in contrast to successful recruitment in FUS WT sMNs (D, gray curves). FUS P525L CN (C, green curves) displayed relatively normal recruitment compared to WT (B, gray curves).

(F) Representative DAB (1st and 3rd panels) and fluorescence immunohistochemistry (IHC, 2nd and 4th panels) were performed on the human motor cortex and lumbar spinal cord using DSB marker γH2AX antibody alone (black arrows in DAB IHC) or in combination with FUS antibody. In FUS-ALS cases, sMNs show consistently strong punctate nuclear staining of γH2AX, whereas most CNs exhibit only mild to moderate γH2AX immunoreactivity (black arrows). Note the appearance of γH2AX accumulations (white arrow) colocalizing with FUS aggregates in both cortical and spinal MNs. Paraffin section: scale bars, 50 μm). (For more details see Figures S2 and S3.)

(G–I) Fluorescence recovery after photobleaching (FRAP) experiments were performed on stress granules (SGs) induced with arsenite.

(G) Representative images of CNs expressing FUS-eGFP WT or P525L mutant, with a representative time series of FRAP images. The arrow indicates a FUS-eGFP-positive SG that was photobleached. Scale bars, 10 μm.

(H) FUS eGFP granule size was generally larger in CNs and increased further in both P525L mutant CNs and sMNs compared to their respective controls.

(I and J) FRAP quantification of arsenite-induced SG, shown as half-time recovery (I) and mobile fraction (J). Mutant sMNs but not CNs showed increased half-time recovery, while there was a generally increased mobile fraction in CNs irrespective of the mutation. $n = 3$ biological replicates; for each condition 49–77 granules were analyzed. Statistical analysis was performed with unpaired two-tailed Student's t test and Welch's correction due to unequal variances. The violin plots represent median with 25th/75th percentile. $^{*}p \leq 0.05$, $^{**}p \leq 0.01$, $^{****}p \leq 0.0001$.

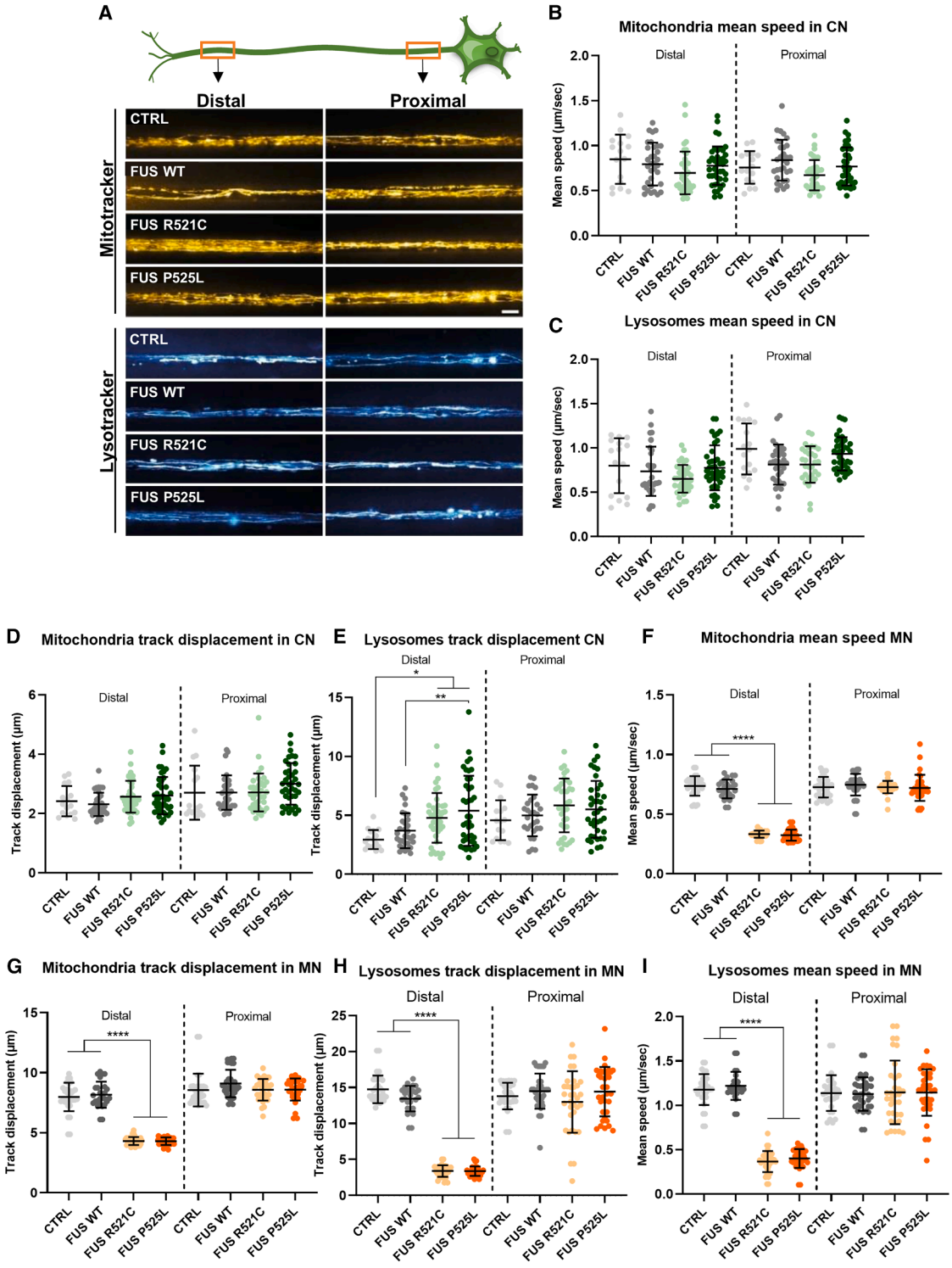

Figure 3. Axonal trafficking defects are much more evident in FUS-ALS spinal motor neurons than in cortical neurons

CNs and sMNs were matured in microfluidic chambers (MFCs) and imaged live at the distal (left) vs. proximal (right) channel end with Mitotracker (yellow hot) and Lysotracker (cyan hot).

(A) Maximum-intensity projections of time-lapse movies reveal tracks of moving organelles in axons of CNs (a side-by-side comparison in Figure S5). Shown are representative single microchannels from the MFC microgroove barrier at either the distal (left) or proximal (right) end, typically containing protruding bundles of

(legend continued on next page)

above, labeled them using live neuronal dye NeuroFluor, and FACS (fluorescence-activated sell sorting) sorted (Figure S6 shows gating). Sorted cells were directly lysed in RNA extraction buffer. Samples were sequenced using next-generation sequencing (NGS) (Figure 4A), and reads were processed to generate normalized counts. We compared libraries using principal component analysis (PCA) (Figure 4B). Principal component 1 (PC1) accounts for 76% of the variance and separates CNs from sMNs, while PC2 accounts for 7% and separates WT from P525L FUS. Since cell-type differences explain most variance, we next performed PCA within each cell type (Figure S7). In both, batch effects separate along PC1, while WT and P525L FUS separate along PC2. We therefore generated four comparisons of differentially expressed genes (DEGs), normalizing for batch effects: (1) WT sMNs vs. WT CNs; (2) P525L sMNs vs. P525L CNs; (3) WT sMNs vs. P525L sMNs; (4) WT CNs vs. P525L CNs. DEGs were considered significant with adjusted $p \leq 0.05$, log2 fold change > 1 or < -1 and false discovery rate 5%.

To validate the identity of cultured neurons, we identified enriched genes in each cell type and analyzed them using Enrichr and the ARCHS4 Tissue Types database. CN samples show enrichment of transcripts typical for bulk brain, different gyri, and cerebral cortex, while sMN samples are enriched for motor neuron and spinal cord transcripts (Figure S8A). To assess whether WT sMNs and WT CNs are similarly mature and able to form synapses, we analyzed expression of classical synaptic markers—piccolo, bassoon, and synapsin 1—and found comparable expression levels in both types (Figure S8B). We further examined neurotransmitter and receptor expression, revealing that CN cultures are mostly glutamatergic, while sMNs express cholinergic markers (Figure S8C).

We next analyzed DEGs between WT and P525L in CNs and sMNs separately. We noticed that FUS mutation has a much greater impact on the sMN transcriptome than on that of the CN (Figures S8D and S8E; full DEG list in Table S4). WT vs. P525L sMN yields 656 DEGs, compared to only 113 in CNs (Figure S8F). Venn analysis shows minimal overlap of only 24 genes between DEGs in CNs and sMNs (Figure S8F), suggesting transcriptional changes are largely cell type specific. Transcriptional differences are also more pronounced between WT CNs and WT sMNs (2,188 DEGs) and even more so between P525L CNs and P525L sMNs (3,364 DEGs) (Figure S8G). Of these, 1,454 are shared across genotypes, while 1,910 are unique to the P525L background (Figure S8G).

We next performed enrichment analysis to identify molecular functions dysregulated by the FUS mutation in CNs and sMNs. In CNs, both up- and downregulated functions include receptor, enzyme, ion channel, and hormone activity (Figure S8H). In sMNs, ion channel activity is downregulated, while microtubule motor activity is upregulated (Figure S8I), suggesting that different cellular processes are affected in each neuronal subtype.

FUS ALS spinal motor neurons, but not cortical neurons, activate the DNA damage response

To better understand the basis of phenotypical differences, we analyzed DEG subsets across conditions. We first identified 1,454 transcripts that differ between CNs and sMNs in the WT background but remain unchanged by mutation (Figure 4C). Enrichment analysis of these physiological DEGs shows upregulation of pathways involving FOXM1, polo-like kinase 1 (PLK1), AuroraA/B, and E2F (Figure 4C). We then focused on 1,910 pathological DEGs—those unchanged in WT CNs vs. sMNs but altered by FUS mutation (Figure 4D). Enrichment again highlights PLK1, AuroraB, FOXM1, and additionally ATR signaling (Figure 4D). To identify potential sMN selective vulnerability factors, we examined transcripts that differ between WT CNs and WT sMNs and are also dysregulated in P525L vs. WT sMNs (Figure 4E). These also show upregulation of PLK1, AuroraB, FOXM1, E2F, and ATR pathways (Figure 4E). Similarly, DEGs altered in sMNs by mutation but not in the WT background show strongest enrichment in PLK1, followed by AuroraA/B and FOXM1 (Figure 4F). These findings indicate that some DNA damage response components are physiologically distinct between CNs and sMNs, and these differences are further enhanced by mutation. Gene set enrichment analysis (GSEA)[20] of WT and P525L FUS sMNs reveals increases in DNA damage sensor activity (GO: 0140612), DNA damage response (GO: 0006974), and positive regulation of cell cycle process (GO: 0090068) (Figure S9), supporting the idea that P525L FUS mutation disrupts DNA damage signaling in sMNs.

Among all identified pathways, PLK1 signaling is consistently enriched across all comparisons. To explore this further, we analyzed the expression of individual PLK1-related transcripts identified in the enrichment analysis. We examined normalized counts of these transcripts in CNs and sMNs across genotypes. Most transcripts are upregulated in WT sMNs vs. WT CNs. While expression remains largely unchanged in CN P525L vs. WT, we observe strong upregulation in sMN P525L vs. WT (Figure 4G), consistent with qPCR validation (Figure S8J).

In contrast, when looking for putative resilience factors in CNs, we found several genes either differing between WT cell types and altered in P525L CN, or unchanged in WT cell types, but affected by mutation in CNs (Figure S10). However, there is no clear pathway enrichment, suggesting that transcriptomic changes in sMNs are the primary drivers of sMN vulnerability.

PLK1 is highly expressed in spinal motor neurons

To further investigate PLK1, we performed immunohistochemistry of healthy control and FUS-ALS cortical and spinal cord tissue. In the motor cortex of healthy controls, PLK1 is detected mainly in lower-layer neurons including Betz cells but shows markedly

5–20 protruding axons. Processive motility appears as straight, longer trajectories, whereas immobile organelles appear as punctate signals. Representative examples from the mutant FUS (Table S1) and control (ctrl) line pools are shown as annotated. Scale bar, 10 μm.
(B–I) Scatter dot plots show quantification of various tracking parameters deduced from movies from (A) as per-movie mean values (i.e., each data point presents one movie) for CNs (B–E) and sMNs (F–I). A one-way ANOVA with a Bonferroni post hoc was utilized to reveal significant differences in pairwise comparisons. Asterisks: highly significant alteration in pairwise comparisons as highlighted by brackets above data, $^{*}p \leq 0.05$, $^{**}p \leq 0.01$, $^{****}p \leq 0.0001$; all other pairwise comparisons were not significantly different. Data on dot plots are presented as mean with SD.

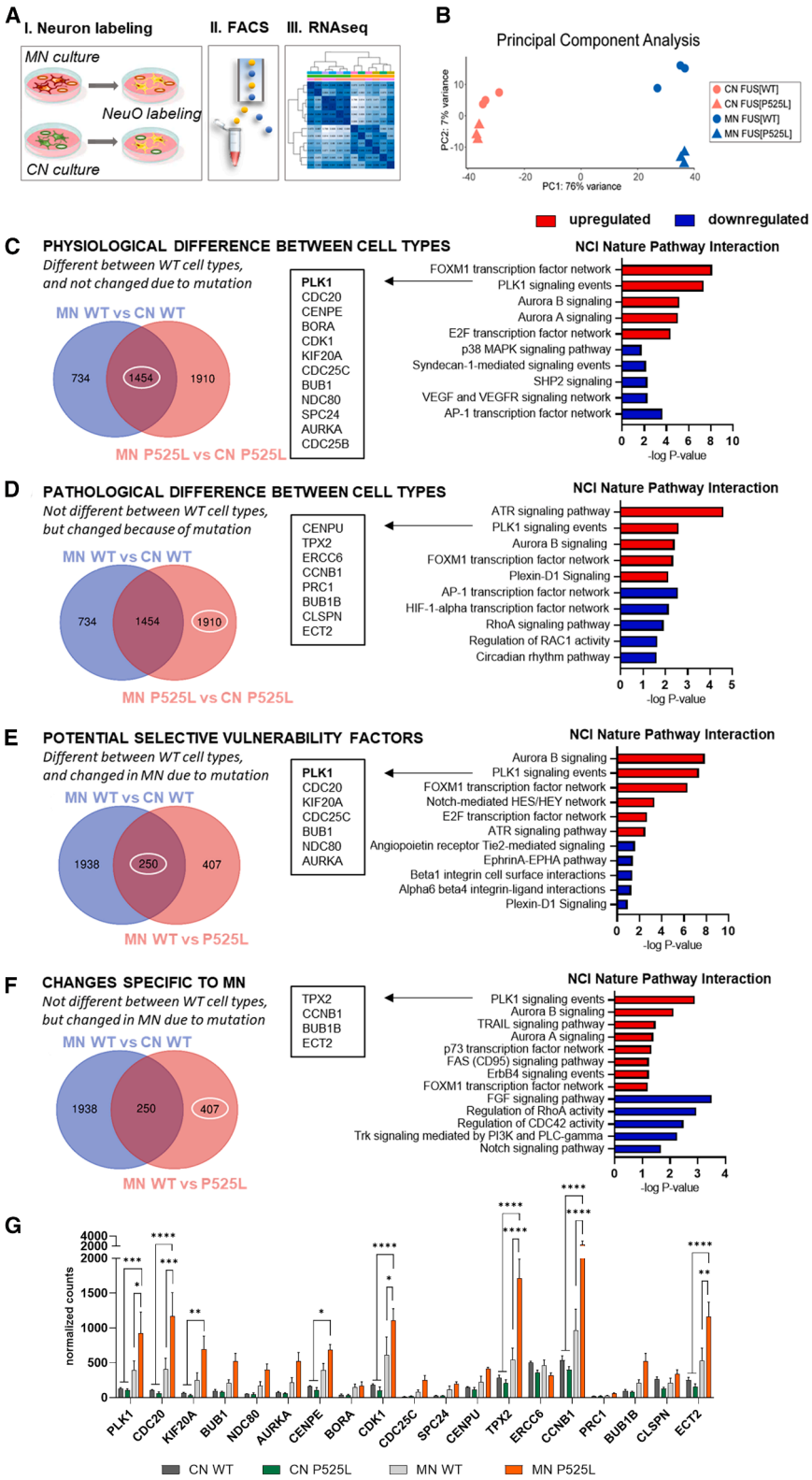

Figure 4. Transcriptomic differences highlight the role of polo-like kinase 1 signaling in spinal motor neurons

(A) Schematic overview of the experimental workflow. Patient-derived CNs and sMNs were differentiated as shown in Figure 1, labeled with the neuron-specific live-cell dye NeuO, and subjected to FACS sorting. RNA-seq was then performed on the NeuO-positive fractions for each neuronal subtype.

(B) Principal component analysis (PCA) of CNs and sMNs with and without the P525L FUS mutation.

(C) Venn diagram (left) shows transcripts differentially expressed in the WT background but unchanged by the mutation. Corresponding enrichment analysis is shown on the right.

(D) Venn diagram (left) shows transcripts expressed differently between CNs and sMNs in the mutant background but not in WT. Enrichment analysis of these transcripts is shown on the right.

(E) Venn diagram (left) and enrichment analysis (right) of transcripts that are differentially regulated between CNs and sMNs in the WT background and are also dysregulated in P525L sMNs compared to sMN WT.

(F) Venn diagram (left) and enrichment analysis (right) of transcripts that are differentially regulated due to FUS mutation in sMNs but not differently expressed between CNs and sMNs in the WT background.

(G) Expression analysis of individual transcripts related to PLK1, identified in the enrichment analysis. Shown are normalized counts of PLK1-associated transcripts across CNs and sMNs in both WT and P525L background. The statistical analysis was performed using two-way ANOVA with post hoc Tukey test. $^{*}p \leq 0.05$, $^{**}p \leq 0.01$, $^{***}p \leq 0.001$, $^{****}p \leq 0.0001$. Data are presented as mean with SD.

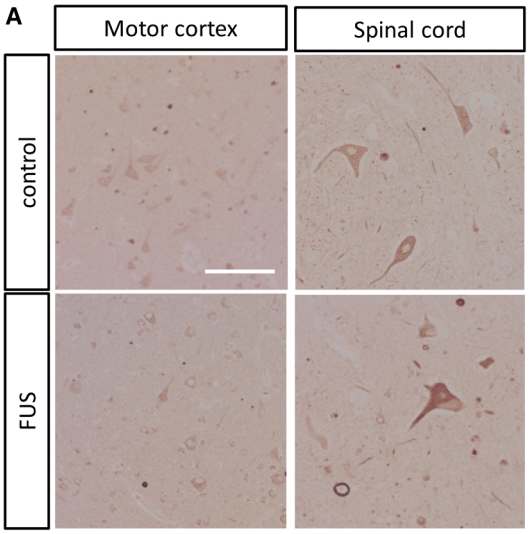

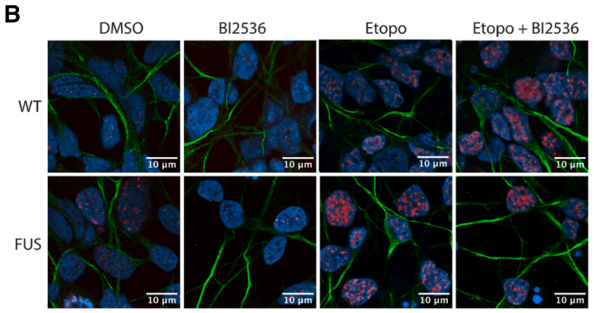

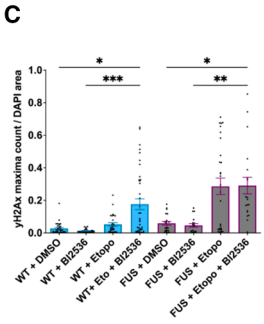

Figure 5. Polo-like kinase 1 is specifically expressed in spinal motor neurons and involved in DNA damage response

(A) Postmortem analysis of FFPE tissue from FUS-ALS cases and respective age- and sex-matched controls. Representative immunohistochemical stainings of deeper cortical layers and the anterior horn are shown. Arrowheads indicate strongly stained neurites.

(B and C) Analysis of DNA damage foci labeled by γH2AX in control and FUS mutant sMNs, treated with DMSO or additionally exposed to etoposide or PLK1 inhibitor BI2536. Representative images are shown in (B), with quantification of γH2AX foci presented as box plot in (C). Data represented as mean ± SEM. N(exp) = 4–5. Significance assessed with one-way ANOVA. $^{*}p \leq 0.05$, $^{**}p \leq 0.01$, $^{***}p \leq 0.001$.

higher expression in sMNs (Figures 5A and S11–S13), fully supporting RNA-seq data. In the anterior horn gray matter, PLK1 is exclusively present in sMNs (Figures 5A and S11–S13). In the spinal cord gray matter, PLK1 is detected in both cell bodies and neurites. Comparison with FUS-ALS tissue reveals a similar distribution of PLK1 in both motor cortex and spinal cord (Figures 5A and S11–S13), further supporting RNA-seq data.

PLK1 activity may be regulated by DNA damage response upregulation and plays a protective role in stress

PLK1 has been increasingly linked to non-cell-cycle functions,[21,22] including roles in DNA damage repair in a poly(ADP-ribose) dependent manner,[23,24] closely paralleling functions attributed recently to FUS.[3] We therefore investigated whether PLK1 activity contributes to DNA damage response mechanisms. As previously reported, we confirmed that P525L FUS sMNs exhibit elevated levels of γH2AX-positive DNA damage foci (Figures 5B and 5C). In unstressed conditions, 24-h treatment with 1 μM PLK1 inhibitor BI2536 causes only a non-significant reduction of γH2AX in both control and P525L FUS sMNs. Upon etoposide challenge, however, both WT and P525L FUS sMN display increased DNA damage, with higher DNA repair foci counts in P525L FUS cells. Notably, PLK1 inhibition further increases DNA damage in etoposide-treated control sMNs, whereas none is observed in P525L FUS sMNs, possibly due to pathway saturation or prior activation. These findings support a protective role of PLK1 in DNA repair and cell survival.

Nuclear loss of FUS is particularly prevalent in spinal motor neurons

Given that DNA damage represents a prominent and upstream difference between CNs and sMNs and that PLK1 signaling implicates DNA damage response pathway involvement in FUS-ALS sMNs, we asked whether altered FUS nuclear-cytoplasmic shuttling contributes to this. To address this, we analyzed iPSC-derived neurons, as postmortem tissue reflects end-stage disease. Notably, FUS expression is higher in CNs than sMNs (Figure 6E). Upon P525L mutation, both CNs and sMNs show a significant reduction in nuclear/cytoplasmic FUS ratio, with more pronounced loss in sMNs (Figures 6A and 6B). While cytoplasmic mislocalization occurs in both cell types, nuclear depletion of FUS is especially evident in sMNs (Figure 6B).

We next correlated FUS recruitment to DNA damage sites upon laser irradiation with nuclear-cytoplasmic distribution. A significant correlation emerges between FUS turnover at damage sites and its nuclear-cytosolic distribution, largely driven by nuclear FUS intensity (Figure 6C). Consequently, P525L FUS sMNs with pronounced nuclear loss of FUS fail to recruit FUS to damage sites.

Given these differences, we examined expression of nucleoporins and nuclear transport receptors. WT CNs and sMNs show comparable levels of these transport factors (Figure 6D); however, P525L mutation leads to significant dysregulation of some, more prominently in sMNs than in CNs (Figures 6F and 6G).

Alternative splicing events in sMNs differ from those in CNs and implicate DNA damage pathways in FUS ALS

Since we observed a striking difference in nuclear FUS level between CNs and sMNs, we investigated whether this correlates

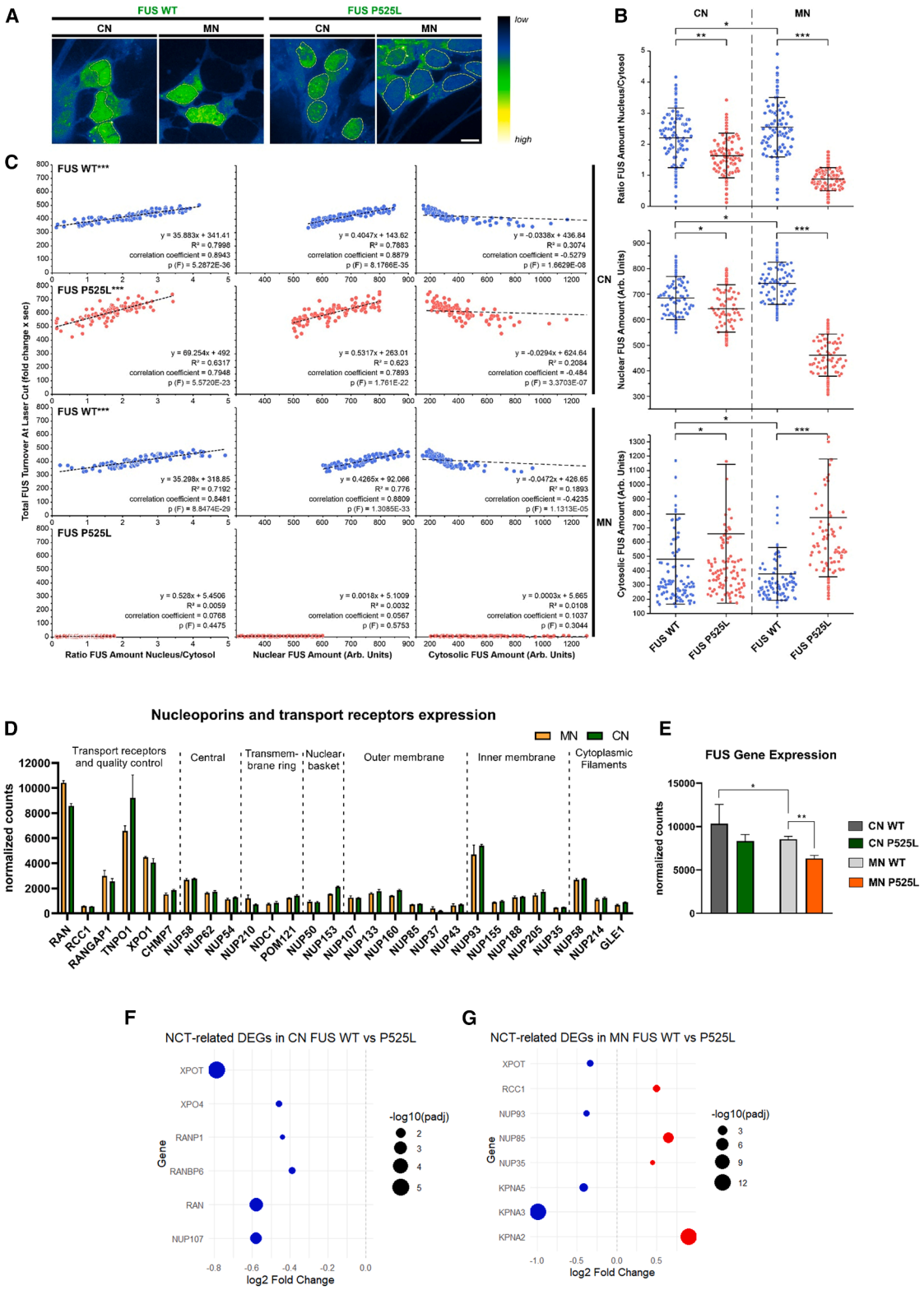

Figure 6. Nucleo-cytoplasmic transport is different in cortical neurons than spinal motor neurons

(A–C) Cytosolic mislocalization of mutant P525L FUS is more pronounced in MNs compared to CNs. (A) Isogenic sMNs or CNs expressing WT or P525L FUS-eGFP (Table S1) were matured for 21 DIV. Shown are maximum-intensity projections of live-imaged confocal z stacks. eGFP intensity is represented using "green

(legend continued on next page)

with cell-type-specific missplicing. FUS is a known splicing factor, and it was shown previously that FUS mutations alter splicing.[5] We first analyzed cassette exon (CE) splicing differences between WT CNs and WT sMNs and identified 134 differentially spliced transcripts (Figure S14A, purple), 115 of which are specific to the WT background (Figure S14A, top). Enrichment analysis reveals that eight of these transcripts have prior association with ALS (Figure S14A, top), suggesting that baseline splicing differences may contribute to selective vulnerability of sMNs. These WT-specific CE events are enriched for genes involved in RNA processing and splicing (Figure S14A, middle).

We next analyzed CE splicing differences between P525L CN and P525L sMN (Figure S14A, pink) and identified 169 differentially spliced transcripts, with only 19 overlapping with the WT comparison (Figure S14A, top). Enrichment analysis indicates that these transcripts are mostly involved in DNA repair (Figure S14A, bottom), suggesting that CE splicing may contribute to differences in the DNA damage response between CNs and sMNs in the FUS mutant background.

We then performed a similar analysis for intron retention (IR) events (Figure S14B). Between WT CNs and WT sMNs, 84 transcripts show differential IR (Figure S14B, top, purple) enriched for genes involved in protein processing and SNARE complex assembly (Figure S14B, middle). In the P525L background, 117 transcripts show differential splicing between CNs and sMNs, with 86 being unique to the mutant condition (Figure S14B, top, pink). These are enriched for RNA processing and protein ubiquitination pathways (Figure S14B, bottom), further highlighting cell-type-specific effects of FUS mutation on splicing.

We then analyzed CE and IR events by neuronal subtype (Figure S14C). In P525L sMNs P525L vs. WT sMNs, CE splicing differences are enriched for transcripts involved in base excision repair—a key pathway for oxidative DNA damage repair in neurons (Figure S14C, top left).[25] IR events in the same comparison are enriched for genes related to ribosome and spliceosome function (Figure S14C, top right). In contrast, P525L CNs vs. WT CNs show CE splicing differences in transcripts involved in cellular senescence, while IR events are primarily linked to regulation of spliceosome (Figure S14C, bottom). These findings suggest that CE splicing alterations may contribute to the heightened vulnerability of sMNs to FUS mutation.

FUS sMNs share differentially expressed genes with other fALS models, including upregulation of PLK1

While all ALS cases are defined by motor neuron degeneration, the extent to which early molecular mechanisms converge remains unclear. A recent study demonstrated that familial ALS (fALS) mutations in *SOD1* (G85R), *PFN1* (G118V), and *TARDBP* (G298S) cause similar transcriptional changes in iPSC-derived motor neurons,[26] including upregulation of DNA damage pathways.[3,4,27] To assess overlap, we compared our P525L FUS sMNs dataset to this study as well as to a dataset comparing *C9ORF72*-ALS sMN with isogenic repeat-corrected controls.[15] We observe substantial overlap: 53% of upregulated and 60% of downregulated genes in P525L *FUS* sMNs are similarly regulated in these datasets (Figure 7A; Table S5).

Given the overlap, we next correlated fold changes between P525L *FUS* and the fALS sMN dataset (G85R *SOD1*, G118V *PFN1*, and G298S *TARDBP* vs. isogenic control),[26] and found a significant positive correlation (Figure 7B; R = 0.33, p = 7.9e−31). Notably, cell cycle genes—including PLK1—cluster in the upper-right quadrant, representing shared upregulation. A similar correlation is observed between P525L FUS and *C9ORF72* sMNs (Figure 7C; R = 0.39, p = 7.5e−55), again with PLK1 and other cell cycle genes among concordantly upregulated set. These findings support the idea of shared molecular mechanisms across different fALS genotypes, including DNA damage, cell cycle activation, and PLK1 upregulation.

DISCUSSION

By systematically comparing patient-derived cortical neurons and spinal motor neurons alongside postmortem tissue, we demonstrate that mutations causing FUS-ALS primarily affect spinal motor neurons. Key pathological features—impaired DNA damage repair, disrupted axonal organelle trafficking, and altered stress granule dynamics—were significantly more pronounced in sMNs than in CNs. RNA-seq revealed a distinct upregulation of several DNA damage and cell cycle regulators in sMNs, with polo-like kinase-1 emerging as a central player. Notably, PLK1 expression is inherently higher in sMNs compared to CNs and is specifically localized to α-MNs in the anterior horn. This expression is further elevated in the presence of FUS mutations. Consistent with its elevated expression, PLK1 contributes to DNA damage repair. Importantly, the upregulation of cell cycle

fire blue" LUT in FIJI: low eGFP intensities appear blue and high intensities green; no nuclear staining was used. Nuclear outlines are indicated with dashed yellow lines. Note the stronger displacement of P525L FUS from the nucleus to the cytosol in MNs versus CNs. Scale bar, 10 μm.

(B) Quantification of nuclear-to-cytosolic FUS-eGFP intensity ratios from (A). n = 100 cells; each data point represents a single cell. Scatter dot plots show median (center line) and standard deviation (whiskers). Statistical analysis: one-way ANOVA with Bonferroni post hoc for normally distributed datasets. Brackets indicate significant pairwise comparisons, $^{*}p \leq 0.05$, $^{**}p \leq 0.01$, $^{***}p \leq 0.001$.

(C) Total area under the curve from nuclear FUS-eGFP recruitment-withdrawal kinetic after laser irradiation (0–850 s; from Figures 2B–2E) plotted against the nuclear-to-cytosolic FUS-eGFP intensity ratio per cell (same dataset as in B). Each point represents a single cell (n = 100). Linear regression (dotted trendline) reveals the correlation coefficient (R^2) and significance (p value from F-statistics). A significant correlation is observed in all conditions except FUS P525L MNs, which failed to recruit FUS to DNA damage sites regardless of its nuclear-cytosolic distribution.

(D) Expression of nucleoporins and transport receptors. Classical nucleoporins and transport receptors were expressed at comparable levels in WT sMNs and WT CNs. Normalized counts are presented, with no statistically significant differences detected between the groups (mean + SEM, n = 3 per group).

(E) MNs showed significantly lower FUS expression than CNs. FUS P525L mutant MNs also exhibited reduced FUS levels compared to WT. Data are presented as normalized counts (mean + SEM, n = 3 per group). Statistical analysis was performed using an unpaired two-tailed t test. Significance: $^{*}p < 0.05$ and $^{**}p < 0.01$.

(F and G) DEGs involved in nucleocytoplasmic transport including nucleoporins and transport receptors in CNs and MNs. Red, upregulated genes; blue, downregulated genes. Significant thresholds: FDR ≤ 10%, adjusted p value ≤ 0.05. Point size represents −log10(adjusted p value).

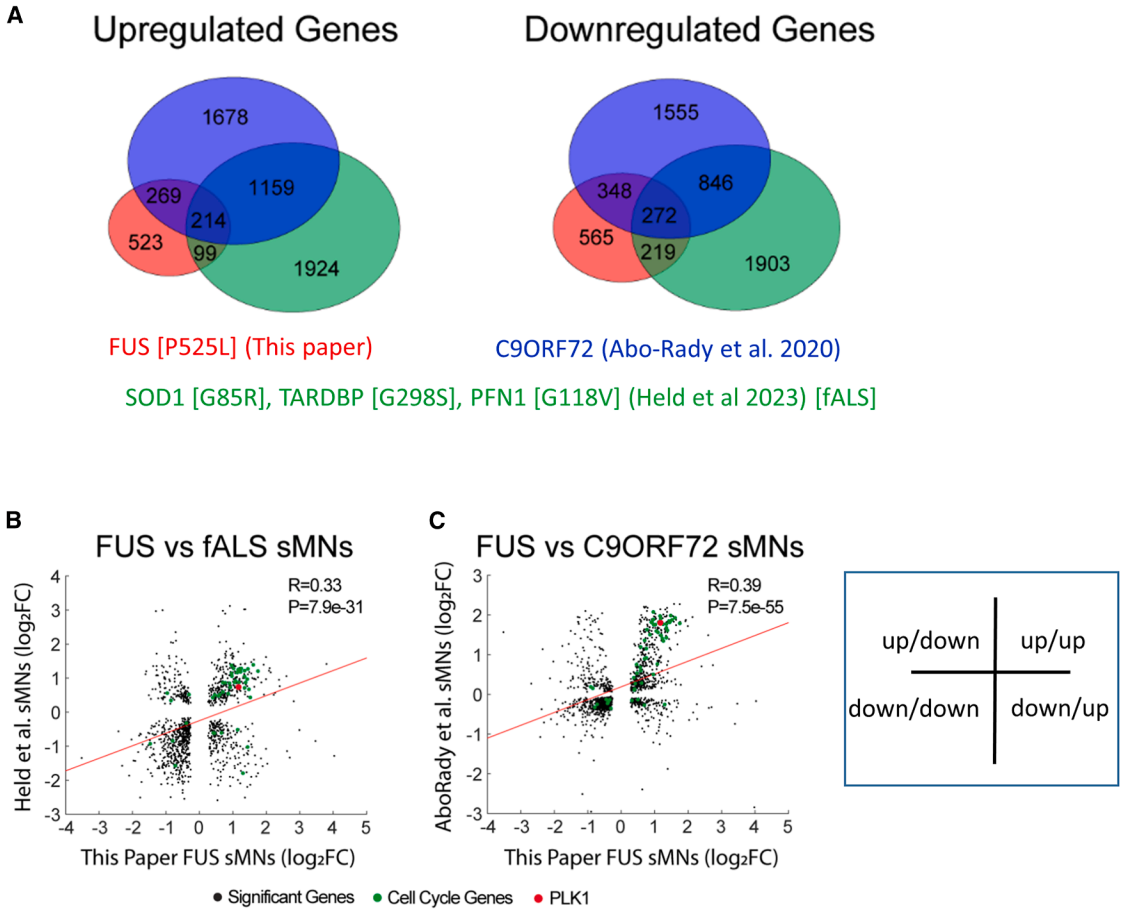

Figure 7. Transcriptomic footprint of P525L FUS motor neurons is similar to other ALS subtypes

FUS P525L sMNs exhibit a DEG profile similar to C9ORF72 and fALS sMNs.

(A) Venn diagrams comparing upregulated and downregulated genes in FUS P525L sMNs, fALS (*SOD1[G85R/+]*, *PFN1[G118V/+]*, and *TARDBP[G298S/+]* vs. isogenic controls), and C9ORF72 sMNs[15] (patient-derived sMNs vs. excised G4C2 repeat controls).

(B) DEGs from FUS P525L sMNs show a significant positive correlation with DEGs from fALS-mutant sMNs.[26] The DEGs from Held et al.[26] were determined by comparing three different fALS lines (*SOD1[G85R/+]*, *PFN1[G118V/+]*, and *TARDBP[G298S/+]*) to their isogenic controls. Each dot represents a gene; cell-cycle-related genes (GO: 0090068) are highlighted in green, and PLK1 is shown in red.

(C) DEGs from FUS P525L sMNs also correlate positively with DEGs from C9ORF72 sMNs.[15] Each dot represents a gene; cell-cycle-related genes (GO: 0090068) are in green, and PLK1 in red.

regulators—including PLK1 expression—is a shared molecular feature of all major fALS forms, including those associated with TARDBP, SOD1 and C9ORF72 mutations.

Amyotrophic lateral sclerosis is characterized by the degeneration of both upper (cortical) and lower (spinal) motor neurons. While most forms of ALS lead to the degeneration of both neuronal populations, FUS-ALS appears to mainly affect lower motor neurons.[9] Furthermore, cognitive dysfunction in FUS-ALS is rare, suggesting a preferential vulnerability of motor neurons over cortical neurons.[28] Our cortical cultures comprise a mixture of upper- and lower-layer neurons (Figure 1); thus, we did not particularly investigate upper motor neurons *in vitro*. Despite this, our data align well with the clinical phenotype, revealing a pronounced involvement of spinal motor neurons and only subtle alterations in cortical neuron—particularly in the early stages of FUS-ALS (Figures 1, 2, and 3).

Unlike other ALS forms linked to TDP43 pathology, FTLD-FUS is a sporadic disease, not associated with mutations in *FUS* gene. Instead, it involves aggregation of WT FUS and is clinically associated with frontotemporal dementia. In contrast, FUS-ALS is caused by mutations in *FUS* and leads to aggregation of both mutant and WT FUS, resulting in motor neuron degeneration.[10,11] Investigating cortical involvement in FTLD-FUS would therefore require a different model systems.

Among the various pathological mechanisms implicated in ALS, DNA damage is a major and well-established feature.[12] FUS plays a critical role in DNA damage repair pathways,[13] including its rapid recruitment to DNA damage sites in a poly(ADP-ribose) (PAR)-dependent manner, as well as in regulating the recruitment of other DNA repair factors.[3,16,17] Notably, FUS interacts directly with HDAC1, a key regulator of DNA repair. However, this interaction is impaired in the presence of FUS-NLS mutations.[29]

As a result, accumulation of DNA damage in spinal motor neurons has thus been shown to play a particularly relevant role in the pathogenesis of FUS-ALS.[3,4] This deficiency appears to be an upstream event that may drive downstream phenotypes, such as impaired axonal organelle trafficking.[3] In our current study, both axonal trafficking and SG dynamics were less affected in CNs, paralleling the milder DNA damage phenotype observed in these cells. This supports the idea of a shared pathophysiological sequence, with DNA damage as a potential initiating factor.

Neuropathological examination of cortical and spinal cord tissue of patients with FUS-ALS further supports this model. While sMNs consistently showed high levels of γH2A.X expression, indicative of severe DNA damage, CNs displayed a more heterogeneous pattern, with fever neurons showing similarly elevated levels (Tables S2 and S3). This contrasts with our iPSC-derived models, where CNs exhibited relatively modest DNA damage phenotypes. However, this discrepancy is expected: postmortem tissue reflects late-stage disease, whereas iPSC-derived neurons are more representative of early pathological changes. Together, these data suggest that DNA damage is differentially regulated in CNs versus sMNs in FUS-ALS, with a more pronounced and earlier onset in sMNs.

The remarkable differences between distinct CNS neurons aligned closely with the clinical phenotypes of FUS-ALS, supporting the utility of our isogenic system for exploring molecular determinants of selective vulnerability. To this end, we FACS-sorted live neurons and performed bulk RNA-seq. Quality control metrics were strong: tissue-specific RNA enrichment and neurotransmitter expression confirmed the accurate identification of cortical vs. spinal neuron identification, while synaptic marker expression indicated comparable maturity between cell types. PCA revealed clear separation based on both cell type and genotype (Figure 4).

Gene expression changes specific to CNs—or indicative of a cortex-specific phenotype—were too few to enable meaningful pathway enrichment analysis, further underscoring that the primary transcriptomic differences arose from sMNs (Figures 4, S7, and S10). Notably, multiple key DEGs were already distinct between WT CNs and sMNs, and these differences were further amplified by the presence of FUS-ALS mutation. These DEGs were primarily involved with DNA damage response and cell cycle regulation. , and included Aurora kinases A and B, FOXM1, and polo-like kinase 1 (PLK1 (Figure 4).

Among all identified pathways, PLK1 signaling emerged as the most prominent. Subsequent postmortem validation confirmed high and selective expression of PLK1 in spinal motor neurons, rather than cortical expression. (Figures 5 and S11–S13). This finding aligns with recent transcriptomic data comparing iPSC-derived cortical neurons with various spinal cord subpopulations, including both motor and sensory neurons.[26] Consistent with our results, that study also found PLK1 expression restricted to sMNs, suggesting that PLK1 may serve not only as a key signaling node in FUS-ALS pathology, but also a potential marker gene or protein for sMNs.

PLK1 is traditionally known for its roles in mitosis, including centrosome maturation, bipolar spindle formation, and cytokinesis. However, like Aurora kinase A and B, PLK1 also performs non-mitotic functions, including DNA damage repair.[30,31] Interestingly, PLK1 is rapidly recruited to double-strand breaks within seconds in a poly(ADP-ribose) polymerase 1 (PARP-1)-dependent manner and disperses within minutes in a PARG-dependent process to promote homologous recombination-mediated repair.[23] FUS exhibits similar kinetic and regulation by PARP1 and PARG.[3,32] This parallel raises the possibility that PLK1 upregulation in FUS-ALS may act as a compensatory response to the nuclear loss of FUS and its impaired recruitment to DNA damage sides. Supporting this idea, PLK1 inhibition in control sMNs treated with etoposide led to a marked increase in γH2AX foci. However, this effect was not observed in P525L FUS sMNs, possibly due to earlier activation or saturation of this pathway in mutant cells (Figure 5B). These findings further support a protective role of PLK1 in DNA damage repair and cell survival. Notably, a recent CRISPR/Cas9 screen in human iPSC-derived cortical neurons identified NEK6 as a novel disease modifier of C9orf72 poly(PR) toxicity, with NEK6 inhibition partially rescuing p53-related DNA damage.[33] PLK1 is known to activate NEK9, which in turn regulates NEK6,[34] suggesting a possible link between PLK1 signaling and DNA damage modulation in ALS. However, most PLK1's function in the DNA damage response—particularly its recruitment to damage sites—have so far been described only in mitotic cells. Further studies are needed to clarify its role post-mitotic neurons, where its function remains poorly understood.

We and others have shown that DNA damage is likely to be upstream of axonal phenotypes, including axonal transport deficiencies and axon degeneration.[3,33] However, the mechanistic link between DNA damage and axon degeneration remains incompletely understood. One potential mediator could be neurofilaments. Neurofilament biology is highly dependent on post-translational modifications, especially phosphorylation, by which neurofilament assembly, turnover, and organization is regulated. Interestingly, PLK1 has also been implicated in regulating neurofilament dynamics. PLK1 inhibition was shown to restore neurofilament deposits and axonal phenotypes in Charcot-Marie-Tooth disease type 2E (CMT2E) iPSC-derived neurons.[35] These findings suggest that PLK1 may contribute to axonal pathology via effects on the neurofilament network, although further research is needed to substantiate this potential connection in the context of FUS-ALS.

Mutations in the NLS of FUS disrupt its nuclear-cytoplasmic shuttling. Both CNs and sMNs exhibited a significantly reduced nuclear-to-cytoplasmic ratio of FUS protein in the mutant FUS background. However, this effect was more pronounced in sMNs, where nuclear depletion of FUS was particularly evident (Figures 6A and 6B). A significant correlation was observed between FUS turnover at DNA damage sites and its nuclear-cytoplasmic distribution, primarily driven by the intensity of nuclear FUS (Figure 6C). In sMNs, this nuclear depletion corresponded with a failure to recruit FUS to DNA damage sites. While classical nucleoporins and nuclear transport receptors exhibited comparable expression levels in WT CNs and WT sMNs (Figure 6D), their dysregulation was more extensive in sMNs upon FUS mutation (Figures 6F and 6G). These findings suggest that differential vulnerability to FUS-ALS-associated mutations may stem, at

least in part, from cell type-specific differences in nuclear-cytoplamic transport mechanisms.

While our study highlights the heightened vulnerability of sMNs to FUS mutation and underscores the central role of cell cycle regulators—particularly PLK1—in this process, perhaps the most striking finding is the substantial overlap in DEGs between FUS mutant sMNs and those with C9ORF72 mutantion[15] as well as TARDBP, PFN1, and SOD1 mutations.[26] Remarkably, this overlap persists despite the use of different differentiation protocols. This observation strongly suggests that the neuronal cell type—rather than the specific differentiation protocol—plays a dominant role in shaping the transcriptional landscape. Notably, genes involved in DNA damage response, cell cycle regulation, and particularly PLK1 were consistently upregulated across all three datasets (Figure 7C). Together, these datasets encompass the majority of fALS cases (>50%). The convergence of these transcriptional changes across distinct genetic backgrounds supports existence of shared molecular mechanisms in fALS. Specifically, DNA damage accumulation, aberrant cell cycle activation, and PLK1 upregulation may represent common pathological pathways underlying motor neuron degeneration in multiple ALS subtypes.

Limitations of the study

Our observations support the hypothesis that FUS nuclear-cytoplasmic shuttling might be differentially regulated between CNs and sMNs, which leads to differential affection of sMNs particularly concerning DNA damage repair and missplicing. It is, however, important that this relationship needs to be further validated in larger cohorts. Although it is known that FUS expression is higher in the cerebral cortex than in the spinal cord (e.g., Human Protein Atlas+), it remains difficult at this point to assume the functional consequences of these regional differences in relation to pathology. This is further complicated by the fact that FUS is a tightly autoregulated RNA-binding protein capable of modulating its own expression through multiple feedback loops. Such autoregulation may buffer or mask the direct effects of baseline expression differences across tissues, making it challenging to interpret whether higher or lower FUS expression directly contributes to region-specific vulnerability or pathological outcomes. Therefore, while the observed expression patterns may hold biological relevance, future mechanistic and functional validation is needed.

RESOURCE AVAILABILITY

Lead contact

Further information and requests for resources and reagents should be directed to and will be fulfilled by the lead contact, Andreas Hermann (andreas.hermann@med.uni-rostock.de).

Materials availability

This study did not generate new, unique reagents.

Data and code availability

- RNA-seq data are available at GEO: GSE272827.
- Microscopy data reported in this paper will be shared by the lead contact upon request.
- Any additional information required to reanalyze the data reported in this paper is available from the lead contact upon request.

ACKNOWLEDGMENTS

We acknowledge the great cell culture help of Sylvia Kanzler, Anett Böhme, Katja Zoschke, and Jette Abel. The Light Microscopy Facility (LMF) of CMCB (Center for Molecular and Cellular Bioengineering, Technische Universität Dresden) provided excellent support for all live-imaging experiments. We thank Ronny Sczech for having programmed the original FIJI/KNIME analytical HC organelle trafficking pipeline and J.J. Anink (Amsterdam UMC neuropathology) for technical support. We thank Susann Lehmann for performing histological stains. This work was supported, in part, by the NOMIS foundation to A. Hermann. A. Hermann is supported by the Hermann und Lilly Schilling-Stiftung für medizinische Forschung im Stifterverband. R.G. was supported by niemALSaufgeben.eV and an ALS family. E.A. is supported by ALS Stichting (grant "ALS Tissue Bank – NL"). Part of the work (B.P.D.) was funded by the framework of the Professorinnenprogramm III (University of Rostock) of the German federal and state governments. J.S. is supported by funding from the Technische Universität Dresden.

AUTHOR CONTRIBUTIONS

Conceptualization, B.S. and A. Hermann; data curation, B.S., A.P., D.G., A.V. J., J.J., T.-T.K., H.G., B.P.D., M.B., M.N., and R.G.; formal analysis, B.S., A.P., B.P.D., D.G., A.V.J., M.B., V.Z., K.S., A.D., J.S., E.A., N.A.S., A.B., M.K., H.P., A.G., B.J.W., and A. Held; funding acquisition, A. Hermann; methodology, B. S., A.P., A. Held, and H.G.; project administration, A. Hermann; resources, J. S., E.A., N.A.S., A.B., M.K., H.P., A.G., B.J.W., and A. Hermann; software, A. P., H.G., A. Held, and M.B.; supervision, A. Hermann; validation, B.S., A.P., and A. Held; visualization, B.S., A.P., A. Held, and M.B.; writing – original draft, B.S. and A. Hermann; writing – review & editing, all authors.

DECLARATION OF INTERESTS

A.H. has received personal fees and non-financial support from Biogen and Desitin during the conduct of the study outside of the submitted work. R.G. has received honoraria from Biogen as an advisory board member and for lectures and as a consultant and advisory board member from Hoffmann-La Roche. He also received travel expenses and research support from Biogen. B.J.W. is a consultant and member of the scientific advisory board of Quralis.

STAR★METHODS

Detailed methods are provided in the online version of this paper and include the following:

- KEY RESOURCES TABLE
- EXPERIMENTAL MODEL AND STUDY PARTICIPANT DETAILS
  - Institutional review board statement
  - Informed consent statement
- METHOD DETAILS
  - Experimental model details and cell culture
  - Immunofluorescence staining
  - DNA damage analysis
  - Laser irradiation
  - Fluorescence recovery after photo bleaching
  - Axonal organelle trafficking
  - Image quantification
  - Fluorescence-activated cell sorting of motor neurons and cortical neurons
  - RNA sequencing
  - DEG analysis
  - Reverse transcriptase quantitative polymerase chain reaction (rtqPCR)
  - Diaminobenzidine (DAB) immunohistochemistry
  - Immunohistochemistry (PLK1)
  - Alternative splicing analysis
- QUANTIFICATION AND STATISTICAL ANALYSIS

SUPPLEMENTAL INFORMATION

Supplemental information can be found online at https://doi.org/10.1016/j.celrep.2025.116113.

Received: November 18, 2024
Revised: May 29, 2025
Accepted: July 16, 2025

REFERENCES

1. Dormann, D., and Haass, C. (2013). Fused in sarcoma (FUS): an oncogene goes awry in neurodegeneration. Mol. Cell. Neurosci. *56*, 475–486. https://doi.org/10.1016/j.mcn.2013.03.006.
2. Naumann, M., Peikert, K., Günther, R., van der Kooi, A.J., Aronica, E., Hübers, A., Danel, V., Corcia, P., Pan-Montojo, F., Cirak, S., et al. (2019). Phenotypes and malignancy risk of different FUS mutations in genetic amyotrophic lateral sclerosis. Ann. Clin. Transl. Neurol. *6*, 2384–2394. https://doi.org/10.1002/acn3.50930.
3. Naumann, M., Pal, A., Goswami, A., Lojewski, X., Japtok, J., Vehlow, A., Naujock, M., Günther, R., Jin, M., Stanslowsky, N., et al. (2018). Impaired DNA damage response signaling by FUS-NLS mutations leads to neurodegeneration and FUS aggregate formation. Nat. Commun. *9*, 335. https://doi.org/10.1038/s41467-017-02299-1.
4. Wang, H., Guo, W., Mitra, J., Hegde, P.M., Vandoorne, T., Eckelmann, B. J., Mitra, S., Tomkinson, A.E., Van Den Bosch, L., and Hegde, M.L. (2018). Mutant FUS causes DNA ligation defects to inhibit oxidative damage repair in Amyotrophic Lateral Sclerosis. Nat. Commun. *9*, 3683. https://doi.org/10.1038/s41467-018-06111-6.
5. Lagier-Tourenne, C., Polymenidou, M., Hutt, K.R., Vu, A.Q., Baughn, M., Huelga, S.C., Clutario, K.M., Ling, S.C., Liang, T.Y., Mazur, C., et al. (2012). Divergent roles of ALS-linked proteins FUS/TLS and TDP-43 intersect in processing long pre-mRNAs. Nat. Neurosci. *15*, 1488–1497. https://doi.org/10.1038/nn.3230.
6. Bentmann, E., Neumann, M., Tahirovic, S., Rodde, R., Dormann, D., and Haass, C. (2012). Requirements for stress granule recruitment of fused in sarcoma (FUS) and TAR DNA-binding protein of 43 kDa (TDP-43). J. Biol. Chem. *287*, 23079–23094. https://doi.org/10.1074/jbc.M111.328757.
7. Szewczyk, B., Günther, R., Japtok, J., Frech, M.J., Naumann, M., Lee, H. O., and Hermann, A. (2023). FUS ALS neurons activate major stress pathways and reduce translation as an early protective mechanism against neurodegeneration. Cell Rep. *42*, 112025. https://doi.org/10.1016/j.celrep.2023.112025.
8. Guo, W., Naujock, M., Fumagalli, L., Vandoorne, T., Baatsen, P., Boon, R., Ordovás, L., Patel, A., Welters, M., Vanwelden, T., et al. (2017). HDAC6 inhibition reverses axonal transport defects in motor neurons derived from FUS-ALS patients. Nat. Commun. *8*, 861. https://doi.org/10.1038/s41467-017-00911-y.
9. Nolan, M., Scott, C., Gamarallage, M.P., Lunn, D., Carpenter, K., McDonough, E., Meyer, D., Kaanumalle, S., Santamaria-Pang, A., Turner, M. R., et al. (2020). Quantitative patterns of motor cortex proteinopathy across ALS genotypes. Acta Neuropathol. Commun. *8*, 98. https://doi.org/10.1186/s40478-020-00961-2.
10. Neumann, M., Bentmann, E., Dormann, D., Jawaid, A., DeJesus-Hernandez, M., Ansorge, O., Roeber, S., Kretzschmar, H.A., Munoz, D.G., Kusaka, H., et al. (2011). FET proteins TAF15 and EWS are selective markers that distinguish FTLD with FUS pathology from amyotrophic lateral sclerosis with FUS mutations. Brain *134*, 2595–2609. https://doi.org/10.1093/brain/awr201.
11. Snowden, J.S., Hu, Q., Rollinson, S., Halliwell, N., Robinson, A., Davidson, Y.S., Momeni, P., Baborie, A., Griffiths, T.D., Jaros, E., et al. (2011). The most common type of FTLD-FUS (aFTLD-U) is associated with a distinct clinical form of frontotemporal dementia but is not related to mutations in the FUS gene. Acta Neuropathol. *122*, 99–110. https://doi.org/10.1007/s00401-011-0816-0.
12. Konopka, A., and Atkin, J.D. (2022). DNA Damage, Defective DNA Repair, and Neurodegeneration in Amyotrophic Lateral Sclerosis. Front. Aging Neurosci. *14*, 786420. https://doi.org/10.3389/fnagi.2022.786420.
13. Sukhanova, M.V., Singatulina, A.S., Pastre, D., and Lavrik, O.I. (2020). Fused in Sarcoma (FUS) in DNA Repair: Tango with Poly(ADP-ribose) Polymerase 1 and Compartmentalisation of Damaged DNA. Int. J. Mol. Sci. *21*, 7020. https://doi.org/10.3390/ijms21197020.
14. Mackenzie, I.R.A., Ansorge, O., Strong, M., Bilbao, J., Zinman, L., Ang, L. C., Baker, M., Stewart, H., Eisen, A., Rademakers, R., and Neumann, M. (2011). Pathological heterogeneity in amyotrophic lateral sclerosis with FUS mutations: two distinct patterns correlating with disease severity and mutation. Acta Neuropathol. *122*, 87–98. https://doi.org/10.1007/s00401-011-0838-7.
15. Abo-Rady, M., Kalmbach, N., Pal, A., Schludi, C., Janosch, A., Richter, T., Freitag, P., Bickle, M., Kahlert, A.K., Petri, S., et al. (2020). Knocking out C9ORF72 Exacerbates Axonal Trafficking Defects Associated with Hexanucleotide Repeat Expansion and Reduces Levels of Heat Shock Proteins. Stem Cell Rep. *14*, 390–405. https://doi.org/10.1016/j.stemcr.2020.01.010.
16. Aleksandrov, R., Dotchev, A., Poser, I., Krastev, D., Georgiev, G., Panova, G., Babukov, Y., Danovski, G., Dyankova, T., Hubatsch, L., et al. (2018). Protein Dynamics in Complex DNA Lesions. Mol. Cell *69*, 1046–1061. https://doi.org/10.1016/j.molcel.2018.02.016.
17. Levone, B.R., Lenzken, S.C., Antonaci, M., Maiser, A., Rapp, A., Conte, F., Reber, S., Mechtersheimer, J., Ronchi, A.E., Mühlemann, O., et al. (2021). FUS-dependent liquid-liquid phase separation is important for DNA repair initiation. J. Cell Biol. *220*, e202008030. https://doi.org/10.1083/jcb.202008030.
18. Renger, R., Morin, J.A., Lemaitre, R., Ruer-Gruss, M., Jülicher, F., Hermann, A., and Grill, S.W. (2022). Co-condensation of proteins with single- and double-stranded DNA. Proc. Natl. Acad. Sci. USA *119*, e2107871119. https://doi.org/10.1073/pnas.2107871119.
19. Protter, D.S.W., and Parker, R. (2016). Principles and Properties of Stress Granules. Trends Cell Biol. *26*, 668–679. https://doi.org/10.1016/j.tcb.2016.05.004.
20. Subramanian, A., Tamayo, P., Mootha, V.K., Mukherjee, S., Ebert, B.L., Gillette, M.A., Paulovich, A., Pomeroy, S.L., Golub, T.R., Lander, E.S., and Mesirov, J.P. (2005). Gene set enrichment analysis: a knowledge-based approach for interpreting genome-wide expression profiles. Proc. Natl. Acad. Sci. USA *102*, 15545–15550. https://doi.org/10.1073/pnas.0506580102.
21. Macůrek, L., Lindqvist, A., Lim, D., Lampson, M.A., Klompmaker, R., Freire, R., Clouin, C., Taylor, S.S., Yaffe, M.B., and Medema, R.H. (2008). Polo-like kinase-1 is activated by aurora A to promote checkpoint recovery. Nature *455*, 119–123. https://doi.org/10.1038/nature07185.
22. Kumar, S., Sharma, G., Chakraborty, C., Sharma, A.R., and Kim, J. (2017). Regulatory functional territory of PLK-1 and their substrates beyond mitosis. Oncotarget *8*, 37942–37962. https://doi.org/10.18632/oncotarget.16290.
23. Peng, B., Shi, R., Bian, J., Li, Y., Wang, P., Wang, H., Liao, J., Zhu, W.G., and Xu, X. (2021). PARP1 and CHK1 coordinate PLK1 enzymatic activity during the DNA damage response to promote homologous recombination-mediated repair. Nucleic Acids Res. *49*, 7554–7570. https://doi.org/10.1093/nar/gkab584.
24. Tsvetkov, L., and Stern, D.F. (2005). Phosphorylation of Plk1 at S137 and T210 is inhibited in response to DNA damage. Cell Cycle *4*, 166–171. https://doi.org/10.4161/cc.4.1.1348.
25. Yang, J.L., Chen, W.Y., Mukda, S., Yang, Y.R., Sun, S.F., and Chen, S.D. (2020). Oxidative DNA damage is concurrently repaired by base excision repair (BER) and apyrimidinic endonuclease 1 (APE1)-initiated nonhomologous end joining (NHEJ) in cortical neurons. Neuropathol. Appl. Neurobiol. *46*, 375–390. https://doi.org/10.1111/nan.12584.

26. Held, A., Adler, M., Marques, C., Reyes, C.J., Kavuturu, A.S., Quadros, A.R. A.A., Ndayambaje, I.S., Lara, E., Ward, M., Lagier-Tourenne, C., and Wainger, B.J. (2023). iPSC motor neurons, but not other derived cell types, capture gene expression changes in postmortem sporadic ALS motor neurons. Cell Rep. *42*, 113046. https://doi.org/10.1016/j.celrep.2023.113046.

27. Marques, C., Held, A., Dorfman, K., Sung, J., Song, C., Kavuturu, A.S., Aguilar, C., Russo, T., Oakley, D.H., Albers, M.W., et al. (2024). Neuronal STING activation in amyotrophic lateral sclerosis and frontotemporal dementia. Acta Neuropathol. *147*, 56. https://doi.org/10.1007/s00401-024-02688-z.

28. Grassano, M., Brodini, G., De Marco, G., Casale, F., Fuda, G., Salamone, P., Brunetti, M., Sbaiz, L., Gallone, S., Cugnasco, P., et al. (2022). Phenotype Analysis of Fused in Sarcoma Mutations in Amyotrophic Lateral Sclerosis. Neurol. Genet. *8*, e200011. https://doi.org/10.1212/NXG.0000000000200011.

29. Wang, W.Y., Pan, L., Su, S.C., Quinn, E.J., Sasaki, M., Jimenez, J.C., Mackenzie, I.R.A., Huang, E.J., and Tsai, L.H. (2013). Interaction of FUS and HDAC1 regulates DNA damage response and repair in neurons. Nat. Neurosci. *16*, 1383–1391. https://doi.org/10.1038/nn.3514.

30. Hyun, S.Y., Hwang, H.I., and Jang, Y.J. (2014). Polo-like kinase-1 in DNA damage response. BMB Rep. *47*, 249–255. https://doi.org/10.5483/bmbrep.2014.47.5.061.

31. Ma, H.T., and Poon, R.Y.C. (2020). Aurora kinases and DNA damage response. Mutat. Res. *821*, 111716. https://doi.org/10.1016/j.mrfmmm.2020.111716.

32. Mastrocola, A.S., Kim, S.H., Trinh, A.T., Rodenkirch, L.A., and Tibbetts, R. S. (2013). The RNA-binding protein fused in sarcoma (FUS) functions downstream of poly(ADP-ribose) polymerase (PARP) in response to DNA damage. J. Biol. Chem. *288*, 24731–24741. https://doi.org/10.1074/jbc.M113.497974.

33. Guo, W., Wang, H., Kumar Tharkeshwar, A., Couthouis, J., Braems, E., Masrori, P., Van Schoor, E., Fan, Y., Ahuja, K., Moisse, M., et al. (2023). CRISPR/Cas9 screen in human iPSC-derived cortical neurons identifies NEK6 as a novel disease modifier of C9orf72 poly(PR) toxicity. Alzheimer's Dement. *19*, 1245–1259. https://doi.org/10.1002/alz.12760.

34. Bertran, M.T., Sdelci, S., Regué, L., Avruch, J., Caelles, C., and Roig, J. (2011). Nek9 is a Plk1-activated kinase that controls early centrosome separation through Nek6/7 and Eg5. EMBO J. *30*, 2634–2647. https://doi.org/10.1038/emboj.2011.179.

35. Maciel, R., Correa, R., Bosso Taniguchi, J., Prufer Araujo, I., and Saporta, M.A. (2020). Human Tridimensional Neuronal Cultures for Phenotypic Drug Screening in Inherited Peripheral Neuropathies. Clin. Pharmacol. Ther. *107*, 1231–1239. https://doi.org/10.1002/cpt.1718.

36. Reinhardt, P., Glatza, M., Hemmer, K., Tsytsyura, Y., Thiel, C.S., Höing, S., Moritz, S., Parga, J.A., Wagner, L., Bruder, J.M., et al. (2013). Derivation and expansion using only small molecules of human neural progenitors for neurodegenerative disease modeling. PLoS One *8*, e59252. https://doi.org/10.1371/journal.pone.0059252.

37. Glaß, H., Pal, A., Reinhardt, P., Sterneckert, J., Wegner, F., Storch, A., and Hermann, A. (2018). Defective mitochondrial and lysosomal trafficking in chorea-acanthocytosis is independent of Src-kinase signaling. Mol. Cell. Neurosci. *92*, 137–148. https://doi.org/10.1016/j.mcn.2018.08.002.

38. Japtok, J., Lojewski, X., Naumann, M., Klingenstein, M., Reinhardt, P., Sterneckert, J., Putz, S., Demestre, M., Boeckers, T.M., Ludolph, A.C., et al. (2015). Stepwise acquirement of hallmark neuropathology in FUS-ALS iPSC models depends on mutation type and neuronal aging. Neurobiol. Dis. *82*, 420–429. https://doi.org/10.1016/j.nbd.2015.07.017.

39. Dobin, A., Davis, C.A., Schlesinger, F., Drenkow, J., Zaleski, C., Jha, S., Batut, P., Chaisson, M., and Gingeras, T.R. (2013). STAR: ultrafast universal RNA-seq aligner. Bioinformatics *29*, 15–21. https://doi.org/10.1093/bioinformatics/bts635.

40. Patro, R., Duggal, G., Love, M.I., Irizarry, R.A., and Kingsford, C. (2017). Salmon provides fast and bias-aware quantification of transcript expression. Nat. Methods *14*, 417–419. https://doi.org/10.1038/nmeth.4197.

41. Trincado, J.L., Entizne, J.C., Hysenaj, G., Singh, B., Skalic, M., Elliott, D.J., and Eyras, E. (2018). SUPPA2: fast, accurate, and uncertainty-aware differential splicing analysis across multiple conditions. Genome Biol. *19*, 40. https://doi.org/10.1186/s13059-018-1417-1.

42. Li, H., and Durbin, R. (2009). Fast and accurate short read alignment with Burrows-Wheeler transform. Bioinformatics *25*, 1754–1760. https://doi.org/10.1093/bioinformatics/btp324.

43. DeLuca, D.S., Levin, J.Z., Sivachenko, A., Fennell, T., Nazaire, M.D., Williams, C., Reich, M., Winckler, W., and Getz, G. (2012). RNA-SeQC: RNA-seq metrics for quality control and process optimization. Bioinformatics *28*, 1530–1532. https://doi.org/10.1093/bioinformatics/bts196.

44. Wu, T.D., and Nacu, S. (2010). Fast and SNP-tolerant detection of complex variants and splicing in short reads. Bioinformatics *26*, 873–881. https://doi.org/10.1093/bioinformatics/btq057.

45. Liao, Y., Smyth, G.K., and Shi, W. (2014). featureCounts: an efficient general purpose program for assigning sequence reads to genomic features. Bioinformatics *30*, 923–930. https://doi.org/10.1093/bioinformatics/btt656.

46. Love, M.I., Huber, W., and Anders, S. (2014). Moderated estimation of fold change and dispersion for RNA-seq data with DESeq2. Genome Biol. *15*, 550. https://doi.org/10.1186/s13059-014-0550-8.

47. Ignatiadis, N., and Huber, W. (2017). Covariate-powered weighted multiple testing with false discovery rate control. J. Royal Stat. Soc. B Stat Meth. *83*, 720–751.

48. Chen, E.Y., Tan, C.M., Kou, Y., Duan, Q., Wang, Z., Meirelles, G.V., Clark, N.R., and Ma'ayan, A. (2013). Enrichr: interactive and collaborative HTML5 gene list enrichment analysis tool. BMC Bioinformatics *14*, 128. https://doi.org/10.1186/1471-2105-14-128.

49. Korotkevich, G., Sukhov, V., Budin, N., Shpak, B., Artyomov, M.N., and Sergushichev, A. (2021). Fast gene set enrichment analysis. Preprint at bioRxiv. https://doi.org/10.1101/060012.

50. Burkhardt, M.F., Martinez, F.J., Wright, S., Ramos, C., Volfson, D., Mason, M., Garnes, J., Dang, V., Lievers, J., Shoukat-Mumtaz, U., et al. (2013). A cellular model for sporadic ALS using patient-derived induced pluripotent stem cells. Mol. Cell. Neurosci. *56*, 355–364. https://doi.org/10.1016/j.mcn.2013.07.007.

51. Zhou, Y., Zhou, B., Pache, L., Chang, M., Khodabakhshi, A.H., Tanaseichuk, O., Benner, C., and Chanda, S.K. (2019). Metascape provides a biologist-oriented resource for the analysis of systems-level datasets. Nat. Commun. *10*, 1523. https://doi.org/10.1038/s41467-019-09234-6.

52. Xie, Z., Bailey, A., Kuleshov, M.V., Clarke, D.J.B., Evangelista, J.E., Jenkins, S.L., Lachmann, A., Wojciechowicz, M.L., Kropiwnicki, E., Jagodnik, K.M., et al. (2021). Gene Set Knowledge Discovery with Enrichr. Curr. Protoc. *1*, e90. https://doi.org/10.1002/cpz1.90.

53. Ludolph, A., Drory, V., Hardiman, O., Nakano, I., Ravits, J., Robberecht, W., and Shefner, J.; WFN Research Group On ALS/MND (2015). A revision of the El Escorial criteria - 2015. Amyotroph. Lateral Scler. Frontotemporal Degener. *16*, 291–292. https://doi.org/10.3109/21678421.2015.1049183.

54. Yamoah, A., Tripathi, P., Sechi, A., Köhler, C., Guo, H., Chandrasekar, A., Nolte, K.W., Wruck, C.J., Katona, I., Anink, J., et al. (2020). Aggregates of RNA Binding Proteins and ER Chaperones Linked to Exosomes in Granulovacuolar Degeneration of the Alzheimer's Disease Brain. J. Alzheimers Dis. *75*, 139–156. https://doi.org/10.3233/JAD-190722.

55. Tripathi, P., Guo, H., Dreser, A., Yamoah, A., Sechi, A., Jesse, C.M., Katona, I., Doukas, P., Nikolin, S., Ernst, S., et al. (2021). Pathomechanisms of ALS8: altered autophagy and defective RNA binding protein (RBP) homeostasis due to the VAPB P56S mutation. Cell Death Dis. *12*, 466. https://doi.org/10.1038/s41419-021-03710-y.

STAR★METHODS

KEY RESOURCES TABLE

REAGENT or RESOURCE	SOURCE	IDENTIFIER
Antibodies		
MAP2	abcam	#ab5392; RRID: AB_2138153
Islet-1	abcam	#ab109517; RRID: AB_10866454
Hb9	abcam	#ab92606; RRID: AB_10561593
ChAT	abcam	#ab34419; RRID: AB_726869
β-Tubulin III	Covance	#MMS-435P; RRID: AB_2313773
VGLUT1	abcam	#ab272913; RRID:AB_3068553
FoxP2	abcam	#ab16046; RRID: AB_2107107
Ctip2	abcam	#ab18465; RRID: AB_2064130
SatB2	abcam	#ab51502; RRID: AB_882455
53BP1	Novusbio	#NB100-304; RRID: AB_10003037
PLK1	Proteintech	#10305-1-AP; RRID: AB_2877731
Biological samples		
Postmortem tissue	Department of Neuropathology, Amsterdam UMC, University of Amsterdam and New York Brain Bank of Columbia University	This study, see Table S2
Chemicals, peptides, and recombinant proteins		
Accutase	Sigma-Aldrich	Cat#A6964
Activin A	Biomol	Cat# 97394.10
Ascorbic Acid	Sigma-Aldrich	N/A
B27 Supplement, w/o vitamin A	Thermo Fisher Scientific	Cat#12587010
BDNF	Peprotech	Cat# 450-02-10UG
DBcAMP	Peprotech	Cat# 1698950
DMEM/F12 Medium	Thermo Fisher Scientific	Cat# 21331-020
GDNF	Peprotech	Cat# 450-10-10UG
GlutaMAX Supplement	Thermo Fisher Scientific	Cat# 35050061
Laminin	Sigma-Aldrich	Cat# L2020-1MG
Matrigel Matrix	Corning Inc.	Cat# 354234
N2 Supplement	Thermo Fisher Scientific	Cat#17502-048
Neurobasal Medium	Thermo Fisher Scientific	Cat# 21103-049
Penicillin and Streptomycin	Thermo Fisher Scientific	Cat# 15140-122
Poly-L-Ornithine	Sigma-Aldrich	Cat#A-004-C
Purmorphamine	Biomol	Cat# 10009634
Retinoic Acid	Sigma-Aldrich	N/A
Sodium Arsenite	Sigma-Aldrich	Cat#S7400
TGFβ-3	Peprotech	Cat# AF-100-36E-10UG
Etoposide	Sigma-Aldrich	**#E1383**
BI2536	Med Chem Express	#HY-50698
LysoTracker red DND-99	Molecular Probes	#L-7528
Mitotracker Deep Red FM	Molecular Probes	#M22426
NeuroFluor™	STEMCELL Technologies	#01801

(*Continued on next page*)

Continued

REAGENT or RESOURCE	SOURCE	IDENTIFIER
Critical commercial assays		
miRNeasy Mini Kit	Qiagen	#217084
NEBNext Poly(A) mRNA Magnetic Isolation Module	NEB	#E7490S
NextSeq High Output 75 Cycles Kit	Illumina	#20024906
Quick-RNA Kit	Zymo Research	#R1054
High-Capactiy cDNA Reverse Transcription Kit	Thermo Fisher Scientific	#4374966
FastStart Essential DNA Green Master	Roche	#06402712001
Deposited data		
RNAseq	https://www.ncbi.nlm.nih.gov/geo/query/acc.cgi?acc=GSE272827	GEO: GSE272827
Experimental models: Cell lines		
Human: WT iPSC Ctrl1		Reinhardt et al.[36]
Human: WT iPSC Ctrl2		Reinhardt et al.[36]
Human: WT iPSC Ctrl3		Glass et al.[37]
Human: WT iPSC Ctrl4		Glass et al.[37]
Human: FUS-WT eGFP^{het}		Naumann et al.[3]
Human: FUS-P525L eGFP^{het}		Japtok et al.[38]
Human: FUS R521C^{het}		Naumannet al.[3]
Oligonucleotides		
CGTAGTTCCGACCATAAACGATGCC	Eurofins	18S fwd
GTGGTGCCCTTCCGTCAATTCC	Eurofins	18S rev
TTCGTGTTCGTGGTGTTGGA	Eurofins	PLK1 fwd
TAACTCGGTTTCGGTGCAGG	Eurofins	PLK1 rev
TAACGGCTGAGCTCTTGGA	Eurofins	AURKA fwd
AGGTCCTGAAATGCAGTTTTCTT	Eurofins	AURKA rev
TCGCATCTGGAATGTGTGCT	Eurofins	CDC20 fwd
CCGGGATGTGTGACCTTTGA	Eurofins	CDC20 rev
CCCTTTAGCGCGGATCTACC	Eurofins	CDK1 fwd
AGGAACCCCTTCCTCTTCACT	Eurofins	CKD1 rev
GCCTCTACCTTTGCACTTCCT	Eurofins	CCNB1 fwd
TGTTCTTGACAGTCCATTCACCA	Eurofins	CCNB1 rev
GGGCCTTTCTGGTTCTCTAGTT	Eurofins	TPX2 fwd
TCCTGTAGTCTGGCCTCCTC	Eurofins	TPX2 rev
Software and algorithms		
STAR aligner, version 2.7.1a	https://github.com/alexdobin/STAR	Dobin et al.[39]
Salmon, version 0.14.1	https://github.com/COMBINE-lab/salmon/releases	Patro et al.[40]
SUPPA2 tool, version 2.3	https://github.com/comprna/SUPPA	Trincado et al.[41]
Burrows-Wheeler Aligner v. 0.7.10	https://github.com/lh3/bwa	Li and Durbin[42]
RNA-SeQC v. 1.1.8	https://github.com/francois-a/rnaseqc	DeLuca et al.[43]
FastQC	http://www.bioinformatics.babraham.ac.uk/	http://www.bioinformatics.babraham.ac.uk/
gsnap (v2018-07-04)	https://packages.spack.io/package.html?name=gmap-gsnap	Wu and Nacu[44]
featureCounts (v1.6.3)	https://subread.sourceforge.net/	Liao et al.[45]
DESeq2 R package (v1.24.0)	https://github.com/thelovelab/DESeq2	Love et al.[46]
Independent Hypothesis Weighting package (IHW 1.12.0)	https://github.com/nignatiadis/IHW	Ignatiadis[47]

(*Continued on next page*)

Continued

REAGENT or RESOURCE	SOURCE	IDENTIFIER
Enrichr	https://maayanlab.cloud/Enrichr/	Chen et al.[48]
MATLAB scripts	https://github.com/waingerlab/Szewczyk_etal	https://github.com/waingerlab/Szewczyk_etal
fgsea (1.22.0)	https://github.com/alserglab/fgsea	Korotkevich et al.[49]
GraphPad Prism 7	GraphPad Software Inc.	https://www.graphpad.com/scientific-software/prism/
CellProfiler 2.2.0	Open source (Carpenter et al., 2006)	https://cellprofiler.org/
FiJi ImageJ 2.2.0-rc-65/1.52b	Open source (Schindelin et al., 2009)	https://imagej.net/
KNIME 3.7.2	KNIME AG	https://www.knime.com/

EXPERIMENTAL MODEL AND STUDY PARTICIPANT DETAILS

Patient/proband characteristics is presented in Table S1.

Institutional review board statement

The performed procedures were in accordance with the Declaration of Helsinki (WMA, 1964) and approved by the Ethical Committee of the Technische Universität Dresden, Germany (EK 393122012 and EK 45022009). All procedures involving the use of postmortem tissue samples, were approved by the Ethical Committees of the Academic Medical Center, Amsterdam (W11 073). In the State of New York, research involving autopsy material does not meet the regulatory definition of 'human subject research' and is not subject to institutional review board oversight.

Informed consent statement

Written informed consent was obtained from all participants including for publication of any research results.

METHOD DETAILS

Experimental model details and cell culture

All the hiPSC lines used in this study were previously generated and characterized. Detailed information are presented in the Table S1. The main cell model used in this study were neurons derived from FUS-WT-EGFP and FUS-P525L-EGFP that were generated as a part of previous study.[3] Briefly, fibroblasts carrying R521C FUS mutation obtained from a 58-year-old female were reprogrammed into iPSC using cDNA of OCT4, SOX2, KLF4 and cMYC delivered via retroviral vectors. Next, CRISPR/Cas9 genome editing was used to i) correct the R521C mutation into WT FUS and to tag it with EGFP to generate the FUS WT EGFP line or ii) replace the R521C mutation into P525L FUS mutation and to tag it with EGFP to generate FUS P525L EGFP line.

All hiPSC lines were maintained in feeder-free, animal component-free conditions on the dishes coated with Matrigel (Corning) in mTeSR1 medium (Stemcell Technologies). The cells were regularly split after reaching 60–70% confluence with ReLeSR solution (Stemcell Technologies) according to manufacturer instructions and replated at 1:10–1:50 ratio in mTeSR1 medium with 10 μM Y-27632 inhibitor (abcam).

Differentiation of hiPSC into spinal motor neurons (MNs) was carried out based on the protocol from Reinhardt et al. First, neuronal progenitor cells (NPCs) of ventro-caudal characteristics were derived from hiPSCs as described previously (Naumann et al., 2018). Briefly, hiPSC colonies were detached and suspended in TeSR-E8 medium (Stemcell Technologies) supplemented with 10 μM SB-431542 (Tocris Bioscience), 1 μM dorsomorphin (Tocris Bioscience), 3 μM CHIR 99021 (Cayman Chemical Company) and 0.5 μM purmorphamine (Cayman Chemical Company) to form embryoid bodies (EBs). After two days, medium was changed to N2B27 medium (DMEM-F12/Neurobasal Medium (ThermoFischer Scientific) in a 50:50 ratio, N2 supplement (ThermoFischer Scientific, 1:200), B27 supplement without vitamin A (ThermoFischer Scientific, 1:100), 1% penicillin/streptomycin/glutamine) and aforementioned small molecules at the same concentrations. On day 4, the medium was additionally supplemented with 150 μM ascorbic acid, while SB-431542 and dorsomorphin were withdrawn. On day 6, the EBs were mechanically dissociated and cells were plated on Matrigel-coated plates. The obtained NPCs were then cultivated and further expanded in N2B27 medium supplemented with 3 μM CHIR 99021, 150 μM ascorbic acid and 0.5 μM purmorphamine with regular splittings at a 1:10–1:20 ratio once per week using accutase (Sigma Aldrich) for 10 min at 37°C. To induce differentiation into spinal MNs, NPCs were detached with accutase and replated at a ratio of 1:10 on a Matrigel-coated dish in N2B27 medium supplemented with 0.5 μM purmorphamine, 200 μM ascorbic acid (Sigma Aldrich), 1 μM retinoic acid (Sigma Aldrich), 1 ng/mL BDNF (Promega) and 1 ng/mL GDNF (Sigma Aldrich) (day 0 of differentiation). On day 6, medium was changed to N2B27 supplemented with 1 ng/mL TGFβ-3 (Promega), 100 μM DBcAMP (Sigma Aldrich), 200 μM ascorbic acid, 2 ng/mL GDNF, 2 ng/mL BDNF and 5 ng/mL activin A. On day 7, the culture supernatants were replaced by the

same medium but without activin A. On day 9, cells were detached with accutase and replated in the same medium onto a dish coated with poly-L-ornithine (Sigma Aldrich, 15% in PBS, overnight at 37°C) and laminin (Sigma Aldrich, 1% in PBS put onto the poly-L-ornithine-coated plate overnight at 37°C) at a density of 60,000–75,000 cells/cm^2. For the analysis of axonal organelle trafficking, cells were seeded at day 9 into microfluidic chambers (MFCs) instead as described previously.[3] Briefly, 10 μL of a concentrated cell suspension adjusted to 3x10^7 cells/ml (i.e., 3x10^5 cells in total) were injected into the proximal site of a poly-L-ornithine and laminin-coated MFC in N2B27 medium supplemented only with 100 μM DBcAMP (Sigma Aldrich) and 200 μM ascorbic acid. The medium in the distal site was additionally supplemented with 1 ng/mL TGFβ-3 (Promega), 2 ng/mL GDNF and 2 ng/mL BDNF to maintain a growth factor gradient through the microflow from distal to proximal across the MFC microgroove barrier as a guidance cue for the protruding axons.[3] The matured spinal MNs were kept in their respective final assay format for at least 21 more days with medium refreshments twice per week.

Differentiation of hiPSC into cortical neurons (CN) was based on the protocol published by Burkhardt et al.[38,50] hiPSC were detached and replated at high density on a Matrigel-coated dish in mTeSR1 medium with 10 μM Y-27632 inhibitor. Next day, Y-27632 was withdrawn and the cells were cultivated in mTeSR1 for the next 3-5 days to reach confluent cell layer. After that, neuronal differentiation was induced by applying neuronal differentiation medium (NDM: DMEM-F12/Neurobasal medium at 50:50 ratio, 1% penicillin/streptomycin/glutamine, 1% MEM Non-Essential Amino Acid Solution (ThermoFischer Scientific), 0.5% B27 supplement without vitamin A, 0.5% N2 supplement, 100 μM β-Mercaptoethanol (ThermoFischer Scientific), 5 μg/mL insulin (ThermoFischer Scientific) supplemented with 1.5 μM Dorsomorphin and 10 μM SB-431542. The cells were cultivated for 10 days and on day 11 Dorsomorphin and SB-431542 were withdrawn. The cells were kept in NDM without supplements until day 15 and then 0.05 μM retinoic acid was added. Cell were cultivated like this until day 20. After that, the cells were detached using accutase for 10 min at 37°C and replated on the poly-L-ornithine and laminin-caoted dish at the density of 192,000 cells/cm^2 in NDM supplemented with 0.05 retinoic acid, 2 ng/mL BDNF and 2 ng/mL GDNF. Additionally, only on the day of splitting, 10 μM Y-27632 inhibitor was added. The cells were maintained in these conditions until day 45 and then they were split as previously and replated onto a fresh poly-L-ornithine and laminin-coated dish at a density of 200,000 cells/cm^2 in NDM supplemented with 0.05 retinoic acid, 2 ng/mL BDNF and 2 ng/mL GDNF. Additionally, only on the day of splitting, 10 μM Y-27632 inhibitor was added. The cells were maintained in these conditions until day 45 and then they were finally split for their respective assay and replated onto a fresh poly-L-ornithine and laminin-coated dish in the same medium. For immunofluorescence stainings, laser irradiation, FRAP and FACS for RNA sequencing the obtained CNs were plated at a density of 30,000 cells/cm^2. For the analysis of axonal organelle trafficking, CNs were seeded into MFCs at day 45 as described previously (Naumann et al., 2018). Briefly, 10 μL of a concentrated cell suspension adjusted to 3x10^7 cells/ml (i.e., 3x10^5 cells in total) were injected into the proximal site of a poly-L-ornithine and laminin-coated MFC in NDM medium containing only 0.05 μM retinoic acid. The medium in the distal site was additionally supplemented with 2 ng/mL BDNF and 2 ng/mL GDNF. The matured CNs were kept in culture in their respective final assay format until at least day 90 with medium refreshments twice per week. The cells were regularly tested for mycoplasma contamination.

Immunofluorescence staining

For immunofluorescence staining, the cells were seeded on a glass coverslip or in μ-slide chambered coverslips (ibidi). To fix the cells, they were treated with 4% ice-cold paraformaldehyde in PBS for 10 min. Next, the membrane permeabilization was carried out by incubating the cells with 0.2% Triton X-100 in PBS for 10 min at room temperature. The unspecific binding sites were blocked by treating the cells with blocking buffer containing 1% BSA, 5% donkey serum, 0.3 M glycine, and 0.02% Triton X-100 in PBS for 1 h at room temperature. Next, the primary antibody staining was performed by applying the dilution of desired primary antibodies in blocking buffer and incubating overnight at 4°C. After that, the cells were washed three times for 5 min with PBS and the dilution of secondary antibodies in blocking buffer was applied. The cells were then incubated for 1 h in room temperature followed by three 5-min washing steps with PBS. Nuclei were stained using 0.75 μL/mL Hoechst 33342 (ThermoFischer Scientific) and the coverslip was mounted on the microscope slide using Fluoromount medium (SouthernBiotech). The following antibodies were used: MAP2 (abcam, #ab5392, 1:10.000), Islet-1 (abcam, #ab109517, 1:200), Hb9 (abcam, #ab92606, 1:200), ChAT (abcam, #ab34419, 1:200), β-Tubulin III (Tuj1) (Covance, #MMS-435P, 1:1000); VGLUT1 (abcam, #ab272913, 1:500); MAP2 (abcam, #ab5392, 1:2000); FoxP2 (abcam, #ab16046, 1:1000); Ctip2 (abcam, #ab18465, 1:1000); SatB2 (abcam, #ab51502; 1:600); 53BP1 (Novusbio, #NB100-304, 1:1000). The imaging was performed with Axiovert 200M fluorescence microscope with optical sectioning (Carl Zeiss) using 63x lens with oil immersion or 40x lense with air immersion.

DNA damage analysis

To induce DNA damage, cortical neurons were treated with 2 μM etoposide for 1 h. The cells were fixed immediately after the treatment or left to recover for 24 h and then fixed. PLK1 inhibitor treatment: neurons were differentiated from iPCS-derived NPCs as described above and were treated with 1 μM BI2536 for 24 h, 2 μM Etoposide for 1 h, or with the equivalent volume of DMSO. Next, the cells were immunostained using 53BP1 antibody (Novusbio, #NB100-304, 1:1000) as a DNA double-strand breaks marker and MAP2 (abcam, #ab5392, 1:2000) as a neuronal marker. The imaging was performed with Axiovert 200M fluorescence microscope with optical sectioning (Carl Zeiss) using 63x lens with oil immersion. Quantification of DNA double-strand breaks was carried out with a semi-automated workflow in CellProfiler image analysis software. First, nuclei were identified using Hoechst staining and neuronal bodies were identified using MAP2 staining. MAP2-positive nuclei were then selected manually. Next, 53BP1 foci were

automatically detected and quantified in MAP2-positive nuclei using 53BP1 staining and the results were exported to excel spreadsheet for further analysis.

Laser irradiation

Spinal MNs and CNs were obtained, cultured and differentiated as described above. To perform the DNA-damage-laser irradiation assay, a final split was performed on both cell types to obtain cell cultures in the final assay format in 3.5cm dishes (FluoroDish with 160 μm cover glass bottom, World Precision Instruments) at 3 x 10^5 cells per dish. All subsequent imaging of nuclear DNA damage response to laser irradiation sites was performed as described previously.[3] In brief, a focused 355 nm UV laser beam was directed through a stereotactic galvanometric mirror box to desired x-y-z-positions in cell samples held on a standard inverted Axio Observer Z1 Zeiss microscope equipped with a motorized stage and a piezo-electric Z-actuator. A Zeiss alpha Plan-Fluar 100 ×1.45 oil immersion objective was used and 24 laser shots in 0.5μm-steps were administered over 12μm linear cuts located within cell nuclei. The cellular response to this DNA damage comprised a fast recruitment of FUS-eGFP to the laser cut site followed by its slower withdrawal (on-off kinetics) and were recorded live over at least 15 min by confocal spinning disc imaging of the eGFP tag using a 488 nm laser line and a 12-bit Andor iXON 897 EMCCD camera (512 × 512, 16 μm pixels, 229.55 nm/pixel at 100X magnification) at initial 1 fps and later 0.2 fps during the slower withdrawal phase. All image frames of the obtained movie stacks presented in this report are shown in the look-up-table (LUT) ''Green Fire Blue'' provided in the FIJI software, i.e., low eGFP intensities are shown in blue and high intensities in green shades. No additional HOECHST or alike staining was performed.

Fluorescence recovery after photo bleaching

Fluorescence Recovery after Photobleaching (FRAP) was analyzed as previously described.[7] Briefly, neurons were treated with 200 μM sodium arsenite for 1 h before the analysis to induce formation of cytosolic FUS-EGFP granules. The live cell imaging was carried out with spinning disc IX81 microscope with FRAPPA unit and 63x lens with water immersion. The eGFP signal of selected granules was photobleached with a 488 nm laser at 100% power and dwell time of 50 ms repeated 3 times over the same area. Following that, the imaging of photobleached are was performed at the rate of 10 frames per second until up to 1000 frames were collected. The recovery of the eGFP signal over time was then analyzed using FIJI ImageJ software.

Axonal organelle trafficking

To investigate axonal organelle motility, Ctrl and mutant FUS neurons (Table S1) were matured either as spinal MNs or CNs in MFCs as described above. Time-lapse movie acquisition was performed as described (Naumann et., 2018; Pal et al., 2018). In brief, to track lysosomes and mitochondria, cells were double-stained with live cell dyes LysoTracker red DND-99 (Molecular Probes Cat. No. L-7528) and Mitotracker Deep Red FM (Molecular Probes Cat. No. M22426) at final 50 nM each. Trackers were added from a 1 mM stock in DMSO directly to culture supernatants and incubated for 1 h at 37°C. Live imaging was then performed in the Center for Molecular and Cellular Bioengineering, Technische Universität Dresden (CMCB) light microscopy facility with a Leica HC PL APO 100 ×1.46 oil immersion objective on an inversed fluorescent Leica DMI6000 microscope enclosed in an incubator chamber (37°C, 5% CO_2, humidified air) and fitted to a 12 – bit Andor iXON 897 EMCCD camera (521x512 pixel, 16 μm/pixels on chip, 229.55 nm/pixel at 100× magnification with intermediate 0.7× demagnification in the optical path through the C-mount adapter connecting the camera with the microscope). For more details, refer to https://www.biodip.de/wiki/Bioz06 - Leica AFLX6000 TIRF. Fast dual color movies were recorded at 3.3 frames per second (fps) per channel over 2 min (400 frames per channel in total) with 115 ms exposure time as follows: LysoTracker red (excitation: 561 nm Laser line, emission filter TRITC 605/65 nm) and Mitotracker Deep Red (excitation: 633 nm Laser line, emission filter Cy5 720/60). Dual channel imaging was achieved sequentially by fast switching between both laser lines and emission filters using a motorized filter wheel to eliminate any crosstalk between both trackers.

Organelle tracking analysis was performed on obtained movie stacks as described previously (Naumann et al., 2018; Pal et al., 2018). In brief, organelle recognition and tracking was performed with the FIJI Track Mate plugin which returned the mean speed and track displacement for each organelle type (Mito-versus Lysotracker-labeled). Subsequent data mining of individual per-movie result files was performed in KNIME to assemble final results files with annotated per-organelle parameters, thereby allowing all data from each experimental condition to be pooled (e.g., all data for mitotracker or lysotracker at the distal MFC channel readout position for a given cell line). Mean values per-movie were visualized as scatter dot plots (Figures 3B–3I), i.e., each data point presents one movie. At least five distal and five proximal movies were acquired of each MFC (=one biological replicate) with three MFCs per experiment and three independent experiments (= MN or CN differentiation pipeline) per cell line, typically resulting in at least 45 movies in total per condition.

Image quantification

For cytosolic FUS-eGFP mislocalization in MNs and CNs (Figure S1), maximum intensity projections of confocal Z-stacks acquired by fluorescent live imaging were used for analysis as described previously.[3] In brief, standard segmentation tools of FIJI software were used to measure the fluorescence integral intensity of FUS within the nucleus and cytosol to calculate the ratio nucleus/cytosol. Resultant ratios of nuclear/cytosolic integral intensity were plotted as scatters in which each dot presents one analyzed cell. One hundred cells (N = 100) across at least three independent experiments were analyzed.

Fluorescence-activated cell sorting of motor neurons and cortical neurons

To purify the hiPSC-derived motor and cortical neurons for RNA sequencing, fluorescence-activated cell sorting (FACS) was used. First, neurons were labeled with NeuroFluor NeuO dye (STEMCELL Technologies) with Ex/Em of 468/557 nm that selectively labels neurons in live culture. The dye was diluted in the respective culture medium to the concentration of 0.1 μM and the medium was applied directly to the cells, which were then incubated for 1 h at 37°C. Next, the labeling medium was removed and replaced with fresh culture medium and the cells were incubated for another 90 min. After that, the cells were washed once with PBS and incubated with 0.25% trypsin-EDTA to dissociate. The detached cells were then suspended in PBS with 10% FBS and the suspension was centrifuged at 1200 rpm for 5 min at 4°C. All the following steps were performed on ice. Cell pellet was resuspended at the density of 3x10°6 cells/ml in the sorting buffer containing 4.5 g/L glucose, N2 supplement (1:200), B27 supplement without vitamin A (1:100), 1 mM EDTA, 25 mM HEPES and 10 μM Y-27632 in PBS. Cell suspension was then filtered through the cell strained cap with 35-μm nylon mesh. Shortly before the FACS, propidium iodide was added to the suspension to the final concentration 10 μg/mL to distinguish dead cells. Neurons were sorted using FACS AriaII (BD Biosciences) with 100 μm nozzle. The forward scatter (FSC) and the side scatter (SSC) gating was applied to identify cell debris. FSC height vs. area and SSC width vs. height were used for doublets discrimination. NeuroFluor-positive cells were identified using a set of two filters: 545LP and 560/20 nm. First, propidium iodide-positive cells were gated out using the intensity plot of PE-Texas Red channel vs. 545LP and 560/20 nm channel. The remaining population was plotted as SSC area vs. 545LP and 560/20 nm and the gate for NeuroFluor-positive cells was set based on the negative sample of non-stained cells (See Figure S2 for gating strategy). Using this approach, 150 000 cells were sorted directly into 500 μL of QIAzol Lysis Buffer from miRNeasy Mini Kit (Qiagen). RNA was isolated with miRNeasy Mini Kit following the manufacturer instructions. Such prepared samples were then used for RNA sequencing.

RNA sequencing

Library preparation

Next Generation Sequencing was carried out by Gene Expression/DNA Microarray Facility of MPI-CBG Dresden, Germany. mRNA was isolated from 30 ng total RNA by poly-dT enrichment using the NEBNext Poly(A) mRNA Magnetic Isolation Module (NEB) according to the manufacturer's instructions. Samples were then directly subjected to the workflow for strand-specific RNA-Seq library preparation (Ultra II Directional RNA Library Prep, NEB). For ligation NEB Next Adapter for Illumina of the NEB Next Multiplex Oligos for Illumina Kit were used. After ligation, adapters were depleted by an XP bead purification (Beckman Coulter) adding the beads solution in a ratio of 0.9:1 to the samples. During the following 15 cycles PCR enrichment, unique dual index primer (Truseq design) were incorporated. After two XP bead purifications (with a ratio of 0.9:1 to the sample volume), libraries were quantified using the Fragment Analyzer (Agilent). Libraries were sequenced on an Illumina Nextseq 550 system in 75 bp single-end mode to an average depth of 30 million fragments per library.

Next Generation Sequencing was carried out by Gene Expression/DNA Microarray Facility of MPI-CBG Dresden, Germany. Prior to sequencing, RNA samples quality was validated using Bioanalyzer 2100 and RNA 6000 Pico Kit (Agilent). Samples with quality suitable for RNA sequencing were enriched for mRNA by poly-dT pulldown and the libraries were prepared with Illumina Kit. Single-end RNA sequencing was carried out with NextSeq 500 Illumina Sequencer and the NextSeq High Output 75 Cycles Kit. The average of 29.6 million (SD = 1.4 million) reads of 75 bp were generated per sample. The raw sequencing reads were aligned to the human hg38/GRCh38 reference genome with Burrows-Wheeler Aligner v. 0.7.10 (Li, 2013). The quality of data was assessed with RNA-SeQC v. 1.1.8 (DeLuca et al., 2021). Samples averaged 99.3% alignment to the reference genome (SD = 0.4%) and 1.7% to rRNA regions and an average of 80% (SD = 1.1%) fragments were uniquely aligned to exonic regions. Data normalization and differential expression analysis were carried out using DeSeq2.[46]

DEG analysis

FastQC (http://www.bioinformatics.babraham.ac.uk/) was used to perform a basic quality control of the resulting sequencing data. Fragments were aligned to the human reference genome hg38 with support of the Ensembl 92 splice sites using the aligner gsnap (v2018-07-04).[44] Counts per gene and sample were obtained based on the overlap of the uniquely mapped fragments with the same Ensembl annotation using featureCounts (v1.6.3).[45] Normalization of raw fragments based on library size and testing for differential expression between the different conditions was done with the DESeq2 R package (v1.24.0).[46] PCA was performed with DESeq2 using all samples and then used within cell-type subgroups to investigate additional effects. To identify differentially expressed genes, counts were fitted to the negative binomial distribution and genes were tested between conditions using the Wald test of DESeq2. When comparing P525L versus WT, we included the sample preparation day as a covariate. Resulting p-values were corrected for multiple testing with the Independent Hypothesis Weighting package (IHW 1.12.0).[47] Genes with a maximum of 5% false discovery rate (adjusted p-value $\leq$0.05), unless otherwise specified, were considered as significantly differentially expressed. Gene ontology (GO) and pathway enrichment analyses of candidate genes were carried out by utilizing the Enrichr (https://maayanlab.cloud/Enrichr/) through its web interface.[51,52] Functional enrichment significance was analyzed by using Fisher's exact test with adj p-values and significance was ranked by enrichment score ($-$ log (p-value)). Correlation plots and Venn diagrams of 3 groups were generated using custom MATLAB scripts (https://github.com/waingerlab/Szewczyk_etal). Gene set enrichment analyses were done using fgsea (1.22.0).[20]

Reverse transcriptase quantitative polymerase chain reaction (rtqPCR)

We isolated and purified mRNA using Quick-RNA Kit (Zymo Research, Irvine CA, USA) according to manufactures recommendation. cDNA was generated with the High-Capactiy cDNA Reverse Transcription Kit (Thermo Fisher Scientific, Waltham MA, USA) according to the manufactures recommendations. We carried out the PCR using FastStart Essential DNA Green Master (Roche, Basel, Switzerland) in an LightCycler 480II (Roche, Basel, Switzerland). The cycle regime according to Table S1: PCR cycle regime was performed. Primer pairs (see key resources table) were order from Eurofins Genomics (Ebersberg, Germany) and used at a final concentration of 5 μM. Human postmortem tissue.

The postmortem tissue was obtained within 6–30 h after death (Table S2**).** Human postmortem brain and spinal cord samples fixed in buffered formalin were obtained from the archives of the Department of Neuropathology, Amsterdam UMC, University of Amsterdam and from New York Brain Bank of Columbia University. All patients fulfilled the diagnostic criteria for ALS (El Escorial criteria)[53] as reviewed independently by several neuropathologists. P525L -FUS ALS tissue samples were collected and banked at the New York Brain Bank of Columbia University with consent obtained from the patient's next of kin, according to New York State law and the guidelines of the Department of Pathology of Columbia University and New York Presbyterian Hospital. The controls included in the present study were adult individuals without any history of neurological disease, based on their last clinical evaluation. The demographic details of all the fALS patients together with the normal non-neurological controls included in this study are summarised in Table S2.

Diaminobenzidine (DAB) immunohistochemistry

Paraffin sections (5 μm) were mounted on poly-L-lysine coated slides and placed to dry (37°C overnight) and then processed for immunohistochemistry described in detail elsewhere.[54,55] At first, the sections were deparaffinized in xylene for 20 min and then rehydrated in 100%, 96%, and 70% ethanol for 5 min each followed by endogenous peroxidase quenching (0.3% H_2O_2 in methanol) for 20 min. Antigen retrieval was performed in these sections by heating them in citrate buffer, pH 6 (DAKO), for 20 min in a pressure cooker. After washing in PBS, sections were incubated with primary for 1 h at room temperature or 4°C overnight. After washing in PBS, sections were incubated with the appropriate secondary antibody (ImmunoLogic, Duiven, The Netherlands) for 30 min at room temperature. DAB reagent (ImmunoLogic, ready to use) was used to visualize antibody binding. The sections were then counter-stained with 6% hematoxylin for 3 min. All procedures were performed at room temperature.

Immunohistochemistry (PLK1)

Paraffin-embedded sections are de-waxed, rehydrated, epitopes unmasked by citrate buffer (pH 6.0) and heating in a customary microwave for 10min, washed and permeabilized with PBS-Triton 0.1% for 10min, and blocked in 5% normal goat serum for 60min. The, the sections were incubated overnight with the primary rabbit anti-PLK1 antibody (proteintech, 10305-1-AP) diluted in blocking solution (1:200). The next day, the section were washed in PBS and peroxidase activities were blocked in 0.3% H_2O_2 for 30min. For the visualisation of epitope-primary antibody complexes, we used EnVision polymer secondary antibodies (Dako, Germany). This system is based on a horseradish peroxidise-labelled polymer which is conjugated with secondary antibodies. The labeled polymer does not contain avidin or biotin. Consequently, nonspecific staining resulting from endogenous avidin-biotin activity is eliminated or significantly reduced. Additional negative controls were performed by omitting the primary antibody.

Alternative splicing analysis

RNA-sequencing reads have been mapped to genome and transcriptome (ENSEMBLE genomic resource version: hg38) with STAR aligner,[39] version 2.7.1a. Transcript expression was subsequently quantified with salmon,[40] version 0.14.1 and following that a differential splicing analysis was carried out with SUPPA2 tool,[41] version 2.3. In the following study we focused on two types of alternative splicing events: skipped exons (SE) and retained introns (RI) and we excluded such events which were not quantified in all samples in each contrast. As statistically significant we consider only those events for the the *p*-value of calculated PSI difference was below 0.01 and the magnitude of average PSI difference between conditions was greater than 0.2.

QUANTIFICATION AND STATISTICAL ANALYSIS

For the quantitative analysis, at least 3 independent experiments based on 3 different neuronal differentiation procedures were performed. The statistical analysis was carried out using GraphPad Prism 7.0 software, unless indicated otherwise. A proper statistical test was chosen based on the dataset. The detailed information is provided in the figure legend. All results are reported as mean ± SEM or ±SD. */#$p \leq 0.05$; **/##$p \leq 0.01$; ***/###$p \leq 0.001$; ****/####$p \leq 0.0001$ were considered significant. Data visualization was performed using R (ggplot2 package) and GraphPad Prism 8 (La Jolla).''